ELSEVIER

Physics of the Earth and Planetary Interiors 84 (1994) 111–137

PHYSICS OF THE EARTH AND PLANETARY INTERIORS

Frequency-dependent polarization measurements of long-period surface waves and their implications for global phase-velocity maps

G. Laske [a,*], G. Masters [b], W. Zürn [a]

[a] *IGPP, Scripps Institution of Oceanography, University of California, San Diego, CA 92093, USA*
[b] *Geophysikalisches Institut, Karlsruhe, Germany*

(Received 1 January 1993; revision accepted 6 December 1993)

Abstract

Surface-wave dispersion maps provide important constraints on global models of shear-wave velocity structure. Current surface-wave dispersion maps show significant differences from researcher to researcher, and it is clear that further work is required. In addition to dispersion data, polarization measurements obtained from long-period (100 s or more) three-component recordings from the various global networks can also be used to constrain dispersion maps. The off great circle propagation of the surface-wave packets is relatively easy to interpret within a ray-theoretic framework, and provides sensitivity to higher-order structure. The polarization angles as a function of frequency are readily measured using a multi-taper technique, which also has the benefit of providing an error estimate for the measurements. Application of the technique to three-component seismograms from the global GEOSCOPE array reveals large deviations from great circle propagation (up to 15° for low-orbit Love waves and 10° for Rayleigh waves in the frequency band 5–12.5 mHz). On a more regional scale, an analysis of seismograms from the German Regional Seismic Network (GRSN) reveals even larger, strongly frequency-dependent deviations from great circle propagation in the frequency range 10–50 mHz.

1. Introduction

Recent efforts at modelling the 3D shear-wave velocity structure of the whole mantle using both long-period body waves and free oscillation structure coefficients have demonstrated that large-scale structure can be fairly well resolved in the lower mantle (Masters et al., 1992). On the other hand, the current datasets give relatively poor depth resolution of upper-mantle structure, although the lateral resolution is good. This deficiency can, in principle, be remedied by adding surface-wave dispersion data to the inversion or, equivalently, by modelling long-period surface-wave waveforms (e.g. Woodhouse and Dziewonski, 1984; Woodward et al., 1993). We prefer the use of dispersion data to waveform modelling, as errors are more easily assigned to dispersion data and an independent evaluation of a proper parametrization for upper-mantle structure is possible.

* Corresponding author.

SSDI 0031-9201(94)05029-W

We anticipated that the surface-wave dispersion maps which exist in the literature could be used in our inversions, but we have found that there is considerable variation between the maps of different researchers. For example, a comparison of the Love wave phase velocity maps of Wong (1989) and Montagner and Tanimoto (1990) at a period of 156 s is shown in Fig. 1. The Montagner and Tanimoto map is shown truncated to degree 12 in the middle panel to allow a direct comparison with the Wong map. The amplitude of the Wong map is about a factor of 1.5 times that of the Montagner and Tanimoto map (this is also true at a period of 192 s), and many of the features of the maps are different. Fig. 2 shows the correlation between the two maps at both 156 and 192 s. The correlation is remarkably good until degree 6, but falls off rapidly for higher harmonics. The differences between such maps have led to large differences in the inferred structures, implying profoundly different interpretations of the underlying dynamics (Zhang and Tanimoto, 1992; Su et al., 1992).

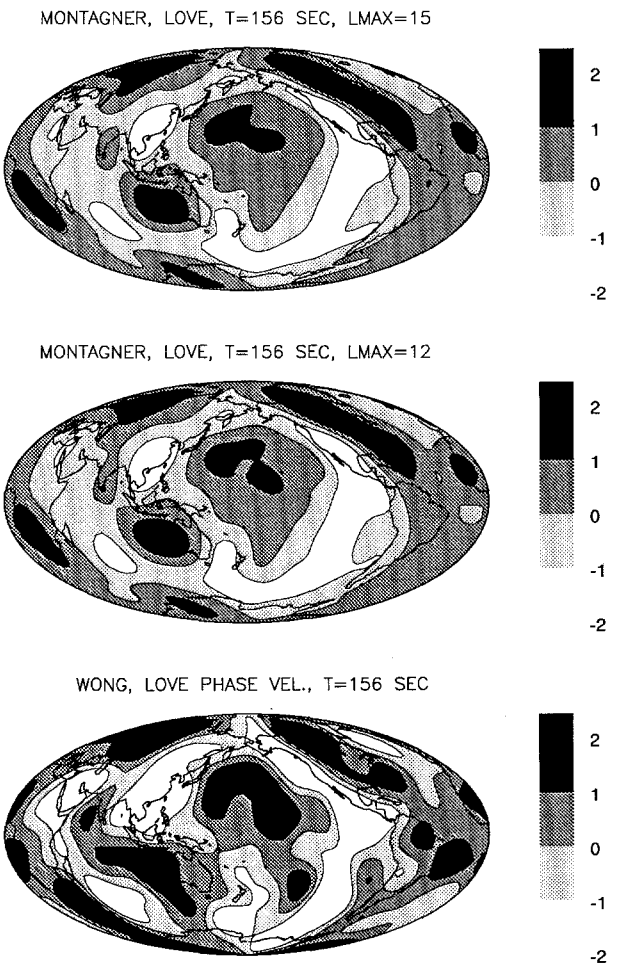

Fig. 1. Love wave phase velocity map (top panel) for a period of 156 s from Montagner and Tanimoto (1990) up to degree 15. For better comparison with Wong's (1989) map (bottom panel), the spherical harmonic expansion has been truncated at $l=12$ in the middle panel. Large-scale characteristics are similar but there is a great difference in amplitude. The maps are percentage perturbations.

It is obviously important to improve our understanding of surface-wave propagation, although it is not clear how much improvement, particularly of short-wavelength structure, can be obtained using classical dispersion analysis. It is well known from previous work (e.g. Masters et al., 1984; Lay and Kanamori, 1985) that long-period surface waves are significantly laterally refracted by heterogeneity in the mantle. The resulting phase and amplitude anomalies have been investigated in the past, and a theoretical framework has been developed for their interpretation (Woodhouse and Wong, 1986). The number of high-quality, long-period three-component seismograms recorded by the various global networks is now sufficiently large to attempt a global analysis of surface-wave polarization. Polarization angles are relatively straightforward to measure and surface-wave ray tracing can be used to interpret such data in terms of a phase velocity map (Woodhouse and Wong, 1986). Polarization analysis can be performed in a real (Jurkevics, 1988) or complex framework (Vidale, 1986), and can be measured as a function of time and frequency (Paulssen et al., 1990). We use the multi-taper technique, which was developed by Park et al. (1987a) and has already been applied successfully in investigations of high-frequency body waves (Park et al., 1987a,b) and for Airy phases of surface waves in the period range 10–30 s (Lerner-Lam and Park, 1989). The method gives an estimate of the quality of the observed signal (in the sense that it can be described by a polarization ellipse) and can suppress bias caused by the presence of incoher-

ent noise—a feature which cannot be implemented in most other techniques.

In the following sections, we describe the multi-taper polarization analysis (MTPA) and introduce a complete formulation for the interpretation of the numerical results in terms of a polarization ellipse oriented arbitrarily in 3D space. The polarization parameters are discussed in detail for two source–receiver configurations of the global GEOSCOPE broadband network (Romanowicz et al., 1984). Ray tracing experiments were carried out for these cases and are compared with the measurements. Polarization angles were measured for 81 events recorded on the GEOSCOPE network and are compared with ray tracing results using two of Wong's (1989) phase velocity maps. In a regional study of seismograms from the German Regional Seismic Network, a method is introduced which utilizes the dispersive nature of the surface waves to improve the polarization analysis. It is found that this method is extremely useful in investigations of Rayleigh waves on the global scale as well.

2. Polarization analysis: the method

If particle motion is confined to a plane in 3D space, it can be described by the complex polarization vector $\hat{z}$, where the two real vectors $\mathrm{Re}(\hat{z})$ and $\mathrm{Im}(\hat{z})$ span the plane of motion. Following Park et al. (1987b), $\hat{z}$ can be found by investigating the eigenstructure of the spectral density matrix $S(f)$ of a three-component time series $x(t) = (x_1, x_2, x_3)$. The right-handed coordinate system used in this study is defined by the three basis vectors $\hat{e}_1$, $\hat{e}_2$, and $\hat{e}_3$, with $\hat{e}_1$ being vertical and pointing up and $\hat{e}_2$ pointing in the radial direction away from the source (Fig. 3). A smoothed estimate of the spectral density matrix S is $\hat{S}(f)$ (Samson, 1983a,b), where

$$\hat{S}_{ij}(f) = y_i^*(f)\, y_j(f)$$

with $y_j(f)$ being the discrete Fourier transform of the tapered time series $x_j(t)$. Using the multitaper technique of Thomson (1982), each of the three components of a seismogram is multiplied

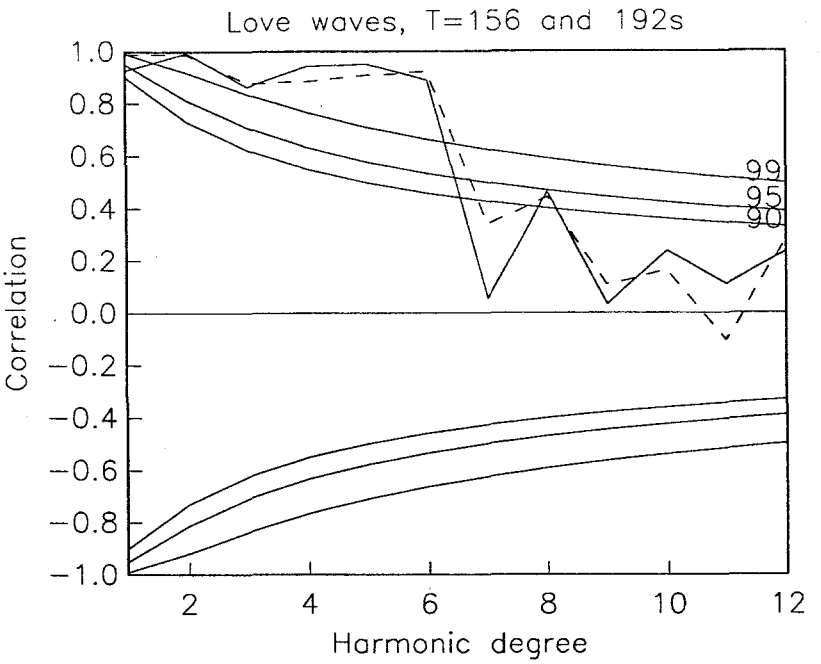

Fig. 2. Correlation between the map of Wong and that of Montagner and Tanimoto as a function of harmonic degree at a period of 156 s (solid line) and 192 s (dashed line). The 99, 95 and 90% confidence levels are also shown. The correlation is very good for low harmonic degrees up to $l = 6$.

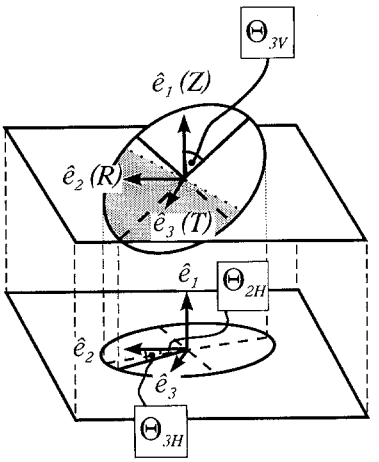

Fig. 3. Polarization ellipse and definition of angles obtained by the MTPA. $\hat{e}_1$, $\hat{e}_2$, $\hat{e}_3$ describe a right-handed coordinate system, with $\hat{e}_1$ pointing up and $\hat{e}_2$ pointing in the radial direction. Θ_{3V} is the angle between the major axis of the polarization ellipse and the vertical, Θ_{3H} is the azimuth of the major axis, measured clockwise from the radial direction (away from the source), and Θ_{2H} is the azimuth of the major axis of the motion in the horizontal plane. Θ_{3H} and Θ_{2H} are, in general, different.

by a taper of the set of K prolate spheroidal wave function eigentapers (Slepian, 1978):

$$y_{k;j}(f) = \frac{1}{N\tau} \sum_{n=0}^{N-1} w_n^{(k)} x_j(n\tau)\, \mathrm{e}^{-in\tau 2\pi f} \qquad (1)$$

where τ is the sampling interval and $w_n^{(k)}$ is the nth value of the kth eigentaper with $0 \leqslant k \leqslant K-1$.

The tapers are the solution to the eigenvalue problem which results from minimizing the spectral leakage outside of a chosen frequency band (see Park et al. (1987a) for details). The number K is defined by the desired resolution in the frequency domain. As the tapers are orthogonal, the K spectral estimates $y_{k;j}$ for component j are independent and the contribution of random, incoherent signals to the final estimate of the polarization parameters is reduced. The spectral estimates $y_{k;j}$ are used to construct a matrix $\boldsymbol{M}(f)$:

$$\boldsymbol{M}(f) = \begin{bmatrix} y_{0;1}(f) & y_{0;2}(f) & y_{0;3}(f) \\ y_{1;1}(f) & y_{1;2}(f) & y_{1;3}(f) \\ \vdots & \vdots & \vdots \\ y_{K-1;1}(f) & y_{K-1;2}(f) & y_{K-1;3}(f) \end{bmatrix}$$

The multi-taper estimate of the 3×3 spectral density matrix is then

$$\hat{S}_M(f) = \frac{1}{K} \boldsymbol{M}^{\dagger}(f) \boldsymbol{M}(f)$$

where the dagger denotes Hermitian transpose.

The eigenstructure of $\hat{S}_M(f)$ is investigated by a singular value decomposition (SVD) of the matrix $\boldsymbol{M}$. For a well-defined polarization, one singular value is much larger than the other two, $d_1 \gg d_2, d_3$ (if normalized, $d_1 \approx 1$; $d_2, d_3 \approx 0$). In this case, the rank of $\hat{S}_M$ is roughly unity and the singular matrix $\hat{S}_M$ can be approximated in a least-squares sense by a vector (Horn and Johnson, 1991, Chapter 7.4) which is the product of the complex right eigenvector $\hat{z}$ corresponding to the largest singular value of $\boldsymbol{M}$ and a complex scaling factor $\mathrm{e}^{i\theta}$, where θ has to be determined. The physical meaning of θ is straightforward. The two real vectors $\mathrm{Re}(\hat{z})$ and $\mathrm{Im}(\hat{z})$ define the plane of motion in real 3D space, but they are not yet aligned with the major and minor axes of the polarization ellipse. These axes are defined as the direction of extremal amplitudes in the plane of motion. The rotation angle θ is chosen to achieve this alignment by maximizing or minimizing (Fig. 4)

$$\left|\mathrm{Re}(\hat{z}\, \mathrm{e}^{i\theta})\right|^2, \qquad \theta = 2\pi f t \qquad (2)$$

As is well-known, polarization parameters are easily interpretable only in the case of a well-defined polarization. A second nonzero singular value, $d_1 \approx d_2 \gg d_3$, is characteristic of the presence of another coherent seismic signal which is orthogonally polarized to the motion corresponding to d_1. Its motion is confined to a plane perpendicular to the plane of the first signal's particle motion. It is clear that this can only be a mathematical model, as we know that different phases (e.g. reflected or refracted phases) or waves of different type are not necessarily orthogonally polarized after travelling in a complicated medium. However, even for the 'well-polarized case', the results have to be interpreted extremely carefully. For example, if two signals of different polarization are stationary or have similar travel times (e.g. multipathing of surface waves), the particle motion of the signals is not separable and

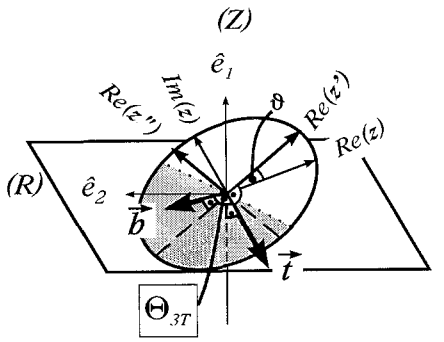

Fig. 4. Location of the polarization vector $\hat{z}$ in the complex plane. The two real vectors $\mathrm{Re}(\hat{z})$ and $\mathrm{Im}(\hat{z})$ span the plane in which particle motion is confined. The tilt Θ_{3T} is defined as the angle between vector $\boldsymbol{b}$ (which is the unit normal vector of the ellipse) and vector $\boldsymbol{t} = Re(\hat{z}') \times \hat{e}_1$ (which lies in the horizontal plane). Vector $\boldsymbol{t}$ can be understood as the location of the vector $\boldsymbol{b}$ of the vertically oriented ellipse before rotation about the major axis by Θ_{3T}.

the SVD will determine only one nonzero singular value and hence one polarization vector which describes the superposition of both signals. Experiments with synthetic seismograms also show that spectral leakage effects might mimic the presence of additional coherent signal. As higher-order tapers suffer more from lack of resistance to spectral leakage, choosing a proper window length and the optimal set of tapers (and an adequate number of tapers) is essential.

If several nonstationary but coherent signals are present in the time interval of interest, techniques have to be found to suppress bias from unwanted signals. Pollitz and Hennet (1993) changed the shape of the tapers to reduce the contribution of Love wave energy when the particle motion of Rayleigh waves is being investigated. This method is very efficient when studying Airy phases. We will show in the regional study that a simple moving window technique is also effective for investigating dispersed signals.

3. Polarization angles, type and quality

In the ideal case of only one nonzero singular value, elliptically polarized motion is the most general model of particle motion, and the two real vectors $\mathrm{Re}(\hat{z})$ and $\mathrm{Im}(\hat{z})$ span the plane in 3D space to which particle motion is confined. The major axis of the polarization ellipse is allowed to have an angle Θ_{3V} with the vertical (Fig. 3). The condition for the orientation of the major axis is Eq. (2) being a maximum.

When considering only two components (e.g. the two horizontal components), the polarization with respect to the plane spanned by these components can be easily determined. The condition for motion in the horizontal plane and the definition of its polarization vector has been given by Park et al. (1987b), and is similar to Eq. (2) with vector $\hat{z}$ being in the horizontal plane. For linear motion, it is clear that the major axis of the degenerate polarization ellipse in the horizontal plane is simply the horizontal projection of the 3D particle motion's major axis. For elliptical motion where $\hat{e}_1$ lies in the plane of motion, the motion in the horizontal plane is degenerate to a linear motion and its azimuth Θ_{2H} is the same as the azimuth of the horizontal projection of the major axis of the ellipse in 3D space, Θ_{3H}. In general, however, when the polarization ellipse is rotated about all three coordinate axes, Θ_{2H} is different from the actual azimuth of particle motion Θ_{3H} (Fig. 3), and measurement of Θ_{3H} is necessary to find the true direction of maximum amplitude of particle motion in 3D space.

To describe fully the orientation of the polarization ellipse we need a third angle, as three angles are necessary for a complete description of the rotation of a rigid body in 3D space. If $\Theta_{3V} \neq 0$, the first two angles are Θ_{3H} and Θ_{3V} and the third is Θ_{3T}, the rotation of the polarization ellipse about its major axis, which is shown in Fig. 4. Let us call this angle the tilt, as it describes the angle between the plane of the particle motion in 3D space and the plane spanned by the vertical and the major axis. It should be noted that Θ_{3H} is not defined and that $\Theta_{3T} = \Theta_{2H}$ when Θ_{3V} is zero. Formally, Θ_{3T} is the angle of the normal of the ellipse, $\boldsymbol{b}$, and a vector $\boldsymbol{t}$, which lies in the horizontal plane ($\boldsymbol{t} \perp \hat{e}_1$) and is perpendicular to the major axis $\mathrm{Re}(\hat{z}')$.

To evaluate the semiaxes of the 3D ellipse, we solve the least-squares problem (2) and define θ_0 as the value for θ closest to zero which imple-

ments $\mathrm{Re}(\hat{z}'_1) < 0$. The vector of the major axis of the polarization ellipse is (Fig. 4)

$$\hat{z}' = \hat{z}\,\exp(-i\theta_0)$$

The minus sign expresses rotation of the coordinate system counter-clockwise so that the axes of the ellipse and the coordinate axes are aligned. The minor axis is

$$\hat{z}'' = \hat{z}\,\exp(-i\theta_1) = \hat{z}\,\exp\left[-i\left(\theta_0 + \frac{\pi}{2}\right)\right]$$

The azimuth of the projection of the major axis onto the horizontal plane, Θ_{3H}, is therefore

$$\Theta_{3H} = \arctan\left[\frac{\mathrm{Re}(z'_3)}{\mathrm{Re}(z'_2)}\right]; \qquad 180° < \Theta_{3H} \leq 180° \tag{3}$$

The angle of the major axis to the vertical, Θ_{3V} is

$$\Theta_{3V} = \arctan\left(\left\{\frac{[\mathrm{Re}(z'_3)]^2 + [\mathrm{Re}(z'_2)]^2}{[\mathrm{Re}(z'_1)]^2}\right\}^{1/2}\right); \qquad 0° \leq \Theta_{3V} \leq 90° \tag{4}$$

The tilt, Θ_{3T}, can be determined by measuring the angle between the normal of the ellipse, $\boldsymbol{b} = (b_1, b_2, b_3) = Re(\hat{z}') \times Re(\hat{z}'')$, and the vector $\boldsymbol{t}$ (where the multiplication sign indicates a cross product). With $\boldsymbol{t} = Re(\hat{z}') \times \hat{e}_1 = [(0, Re(z'_3), -Re(z'_2)]$, the tilt is evaluated by

$$\cos\,\Theta_{3T} = \frac{\boldsymbol{b}\cdot\boldsymbol{t}}{|\boldsymbol{t}|} = \frac{b_2\,\mathrm{Re}(z'_3) - b_3\,\mathrm{Re}(z'_2)}{\left\{[\mathrm{Re}(z'_2)]^2 + [\mathrm{Re}(z'_3)]^2\right\}^{1/2}} \tag{5}$$

after $\boldsymbol{b}$ has been normalized.

The sign of Θ_{3T} is obtained by multiplication with $b_1\mathrm{Re}(z'_1)$ and its range is $-90° < \Theta_{3T} \leq 90°$. The tilt is positive for ellipses rotated to the right when looking down along the major axis. For $\Theta_{3V} = 0$, Θ_{3T} is the ellipse's rotation angle about the vertical axis and $\Theta_{3T} = \Theta_{2H}$.

A useful quantity to estimate the type of polarization is the phase difference, $\Delta\Phi$, between two components as described by Park et al. (1987b). Phase lags close to 0° or ±180° indicate linear motion, and phase lags close to 90° indicate elliptical motion which is oriented parallel to the coordinate system. However, even signals with arbitrary phase lags can be regarded as being linearly polarized if the aspect ratio of particle motion is large enough. Thus the ellipticity, ϵ, appears to be a better parameter to illustrate the type of polarization. For elliptical motion in 3D space, ϵ depends on the moduli of the two vectors $\hat{z}''$ and $\hat{z}'$, and is

$$\epsilon = 1 - \frac{|\mathrm{Re}(\hat{z}'')|}{|\mathrm{Re}(\hat{z}')|} = 1 - \left\{\frac{\sum_{i=1}^{3}[\mathrm{Re}(z''_i)]^2}{\sum_{i=1}^{3}[\mathrm{Re}(z'_i)]^2}\right\}^{1/2} \tag{6}$$

$\epsilon = 1$ indicates linear particle motion, and $\epsilon = 0$ indicates circular motion. Any other value of ϵ indicates elliptical motion.

The quality of polarization is estimated by comparing the singular values d_1, d_2, d_3 of $\boldsymbol{M}$. For a well-defined polarization, the noise-to-signal energy ratio has been characterized by the parameter ρ:

$$\rho = \frac{1 - d_1}{3d_1 - 1}$$

where d_1 is the largest singular value.

Keilis-Borok (1989) and Paulssen et al. (1990) defined a quality function which is a function of ρ, the linearity, and Θ_{3V} in the case of Love waves and a function of ρ, the ellipticity of motion in the radial-vertical plane and Θ_{3V} in the case of Rayleigh waves.

To estimate the type and quality of the signals without any a priori constraints, it is convenient to check the ellipticity ϵ and the errors of the observed polarization parameters. These errors can be derived as formal first-order uncertainties from the first-order uncertainties of the components of $\hat{z}$ (see Park et al., 1987b). It should be emphasized that these first-order estimates, which are derived for a homogeneous and isotropic error model in the data, are valid only for a well-defined polarization, $d_1 \gg d_2$, d_3 and, in general, are probably underestimates of the true uncertainties. The errors do not account for any systematic bias in the polarization angles such as

might be caused by a misalignment of the horizontal components by a few degrees.

4. Polarization measurements of low-frequency seismograms

Good spectral resolution is obviously needed for investigating the frequency dependence of polarization parameters. Three independent spectral estimates in the frequency band 2–12 mHz can be obtained by choosing 2π prolate spheroidal wave function eigentapers with an average window length of 20 min. The first three 2π prolate tapers show better resistance to spectral leakage than the boxcar window (Park et al., 1987a) and are used for the polarization analysis.

A typical example of a three-component long-period seismogram (ZNE filtered to pass the frequency range 3.75–10 mHz) recorded by one of the stations of the GEOSCOPE broadband network (Fig. 5) is shown in Fig. 6. In the record-

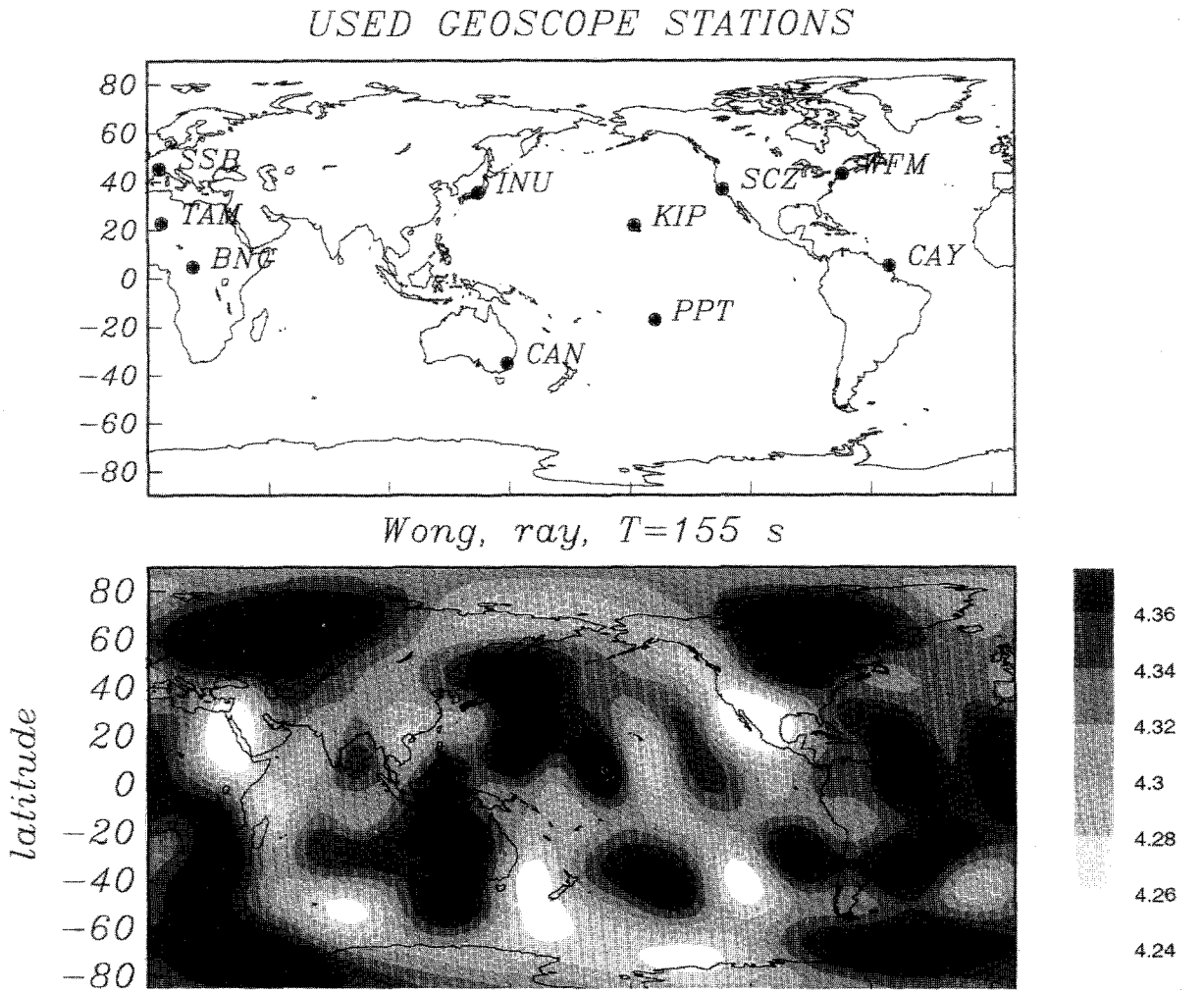

Fig. 5. Wong's (1989) degree-12 phase velocity map for Rayleigh waves at period $T = 155.504s$ (mode ${}_0S_{59}$) and the 10 GEOSCOPE stations used for the comparison between theoretical arrival angles obtained by ray tracing and measurements in Figs. 8, 9 and 10. (The phase velocity is given in km s^{-1}.)

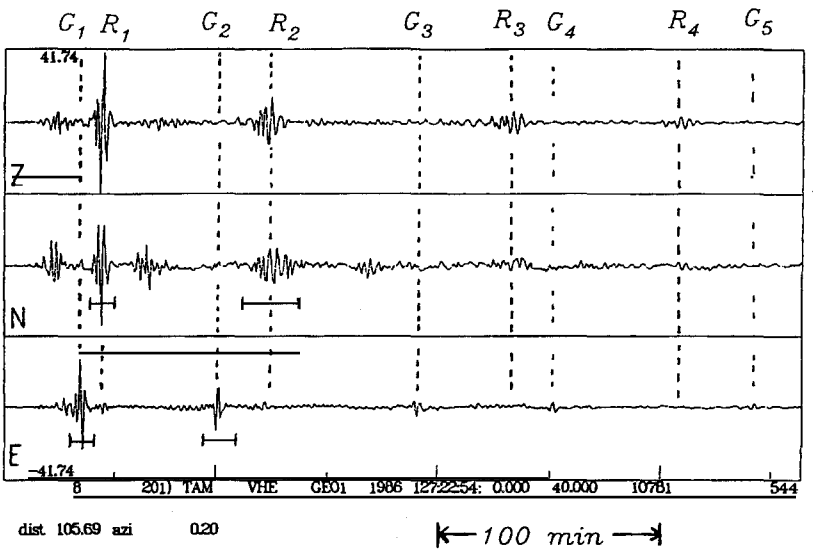

Fig. 6. Aleutians earthquake (7 May 1986, 51.52°N, 174.78°W) recorded at GEOSCOPE Station Tamanrasset, Algeria (TAM). The recording (Z top, N middle, E bottom) is almost naturally polarized with a great circle azimuth of only 0.2°. About 6 h of recording are shown and wave trains G_1–G_5 and R_1–R_4 can be clearly identified. Also shown are the windows (marked by horizontal lines on N and E) used in the MTPA. The windows are 11 min for R_1 and G_1, 15 min for G_2 and 18 min for R_2.

ing, of roughly 6 h length, the wave trains up to G_5 can be clearly identified. The horizontal components are almost naturally oriented (with the N–S component being aligned with the radial direction) for this particular event with a great circle azimuth of only 0.2°. Thus the surface waves are nearly perfectly separated, with Love waves being visible only on the E-component and Rayleigh waves on the Z- and N-components. However, signals occasionally appear on the E-component at the group arrival times of Rayleigh waves, and a weak 'Love wave' can also be observed on the N-component. As the components are naturally oriented, many possible explanations for these observations (such as an inaccurate instrument response) can be rejected, and we can be confident that we are seeing the effects of lateral refraction of the wave packets. It can be seen in Fig. 6 that the windows for R_1 and G_1 can only be about 11 min long and the spectral resolution is not good enough to measure reliably the frequency dependence of the polarization angles. However, owing to their different group velocities, Love and Rayleigh waves are more clearly separated in time for the wave trains of orbit number two. Thus, a window length of 18 min can be used for the polarization analysis of R_2, and gives reasonable spectral resolution.

The results of the MTPA of G_1 and G_2 are plotted in Fig. 7, and those of R_1 in Fig. 8. The largest singular value (d_1) for G_1 in the whole frequency band indicates a well-defined polarization. The 3D ellipticity ϵ is close to unity, showing that the signal is almost linearly polarized, as expected for Love waves, and Θ_{3V} is close to 90°, indicating that the particle motion is limited to the horizontal plane. The measurements of Θ_{3T} have no meaning for linearly polarized motion and are not shown here. With errors of the order of 2–5°, the polarization angle Θ_{3H} shows no significant deviation from the transverse direction and there is no resolvable frequency dependence. In contrast, the polarization angle of G_2 differs significantly from the transverse direction for frequencies greater than 6 mHz and is clearly frequency dependent. The chosen window length of 15 min is large enough to give three independent spectral estimates, so the observed variation is resolvable. In Fig. 8, a large singular value $d_1 \approx 1$ for R_1 implies a well-defined polarization of the

Rayleigh wave. The 3D ellipticity $\epsilon \approx 0.2$ indicates an aspect ratio 1.25:1.00 for the particle motion ellipse, which is in reasonably good agreement with the expected value. The major axis is parallel to the vertical ($\Theta_{3V} \approx 0$). In contrast to Θ_{3H}, the measurements of Θ_{2H} show a stable behaviour and vary only slowly from + 5° to −5° in the frequency band 2–10 mHz. The MTPA results for R_2 are not shown here. Θ_{2H} does not differ significantly from the great circle direction

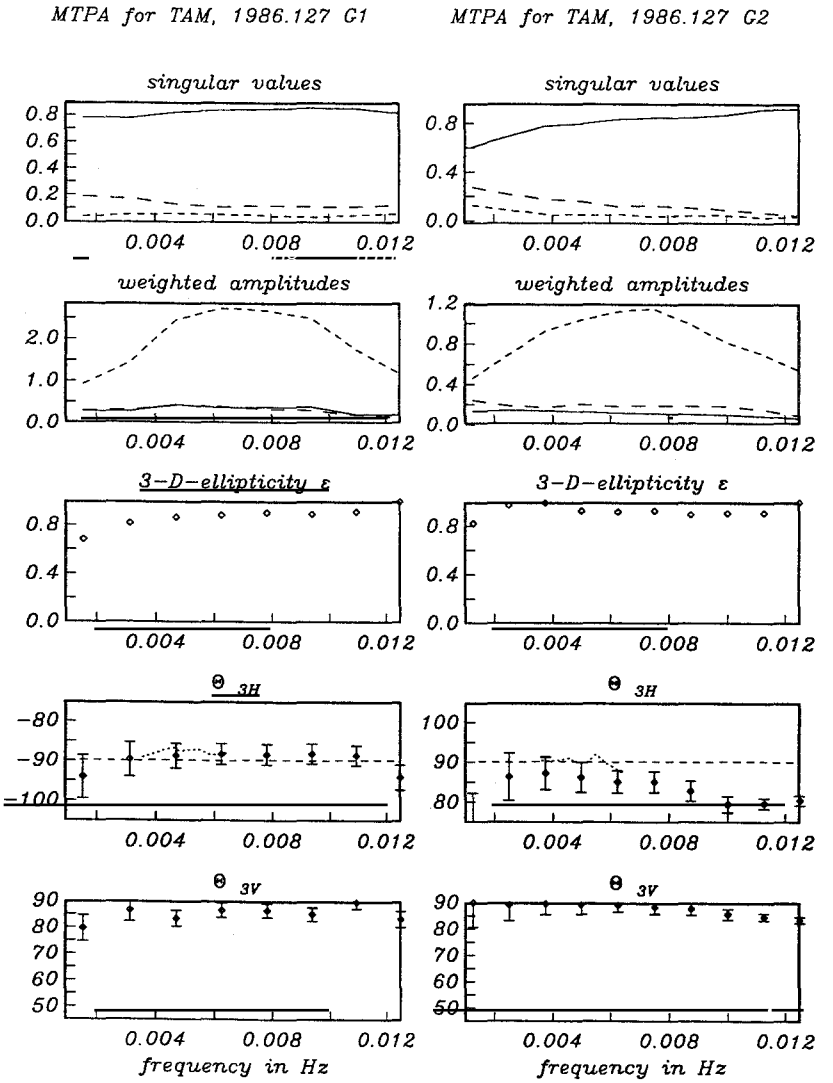

Fig. 7. MTPA results for G_1 and G_2. The large singular values $d_1 \gg d_2$, d_3 for both wave trains indicate the 'well-polarized case'. The angles are shown in degrees. Θ_{3V} is close to 90° and the 3D ellipticity ϵ is close to unity, which implies that particle motion is linear and restricted to the horizontal plane. The anomaly in the horizontal polarization angle Θ_{3H} for G_1 is measured to be about 1° but is not significant. For G_2, Θ_{3H} is weakly dependent on frequency and the anomaly is about 5° on average. Also shown (by dotted lines) are the frequency-dependent polarization angles obtained by ray tracing using Wong's (1989) corresponding phase velocity maps. The weighted amplitudes are the amplitudes of the components after applying the adaptive weighting procedure of Park et al. (1987a) to improve the resistance of the multi-taper method to spectral leakage effects.

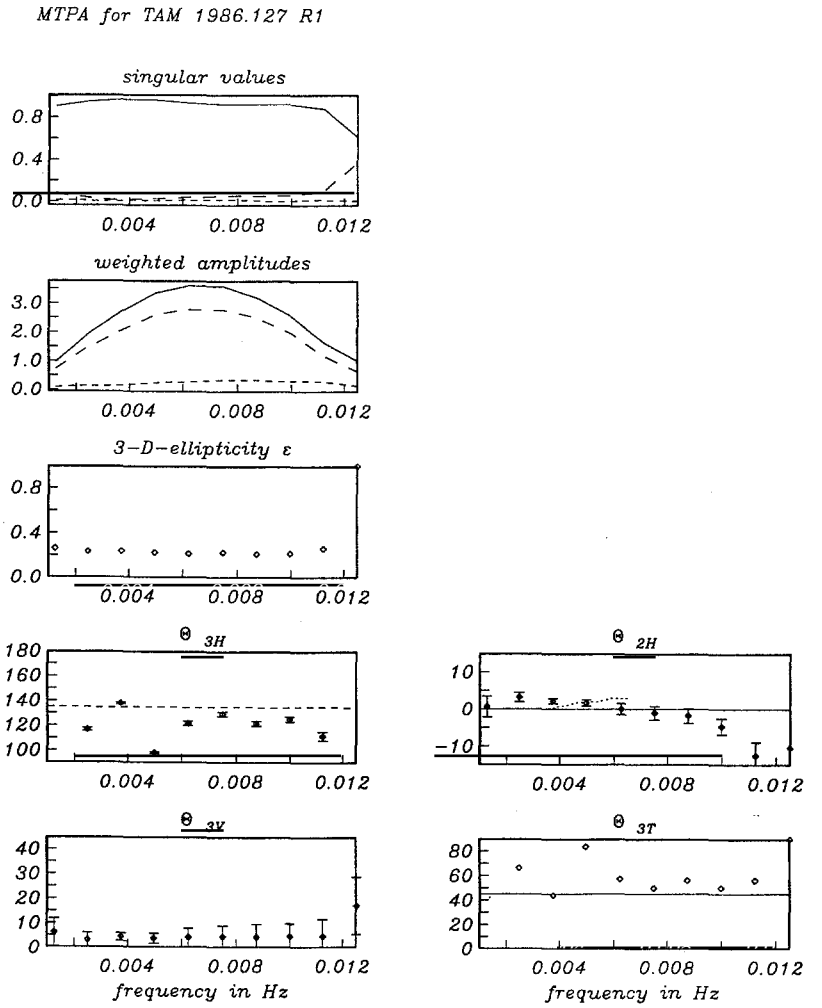

Fig. 8. MTPA results for R_1. (For details, see Fig. 7.) The vertical angle Θ_{3V} is close to 0°, implying that the major axis of the particle motion ellipse is almost parallel to the vertical. The horizontal azimuths Θ_{2H} and Θ_{3H} are different, as the polarization ellipse is rotated about all three coordinate axes. The tilt Θ_{3T} is also shown. This parameter is not defined for linearly polarized signals.

in the whole frequency range, which is in good agreement with ray tracing results as described in the next section and shown in Fig. 9.

It is found that Θ_{3H} measurements are extremely difficult to interpret for Rayleigh waves, and cannot simply be explained by deviations from great circle propagation owing to slowly varying lateral phase velocity heterogeneities. The apparently rapid variations of Θ_{3H} can be partly explained by a complex rotation of the particle motion ellipse not only about the vertical axis, as expected, but also about the ray axis by a small angle. Θ_{2H} is not affected strongly by the latter rotation, but Θ_{3H} and Θ_{3T} change quickly from 0° to 90°. A change in angles of this kind can be seen at about 4 mHz in Fig. 8. Θ_{3H} is also sensitive to the change of the aspect ratio of vertical to horizontal motion, which can be caused simply by a change in vertical velocity structure. In a horizontally layered medium, the vertical and radial displacement can have ratios above or below one, causing Θ_{3V} to be either 0° or 90°,

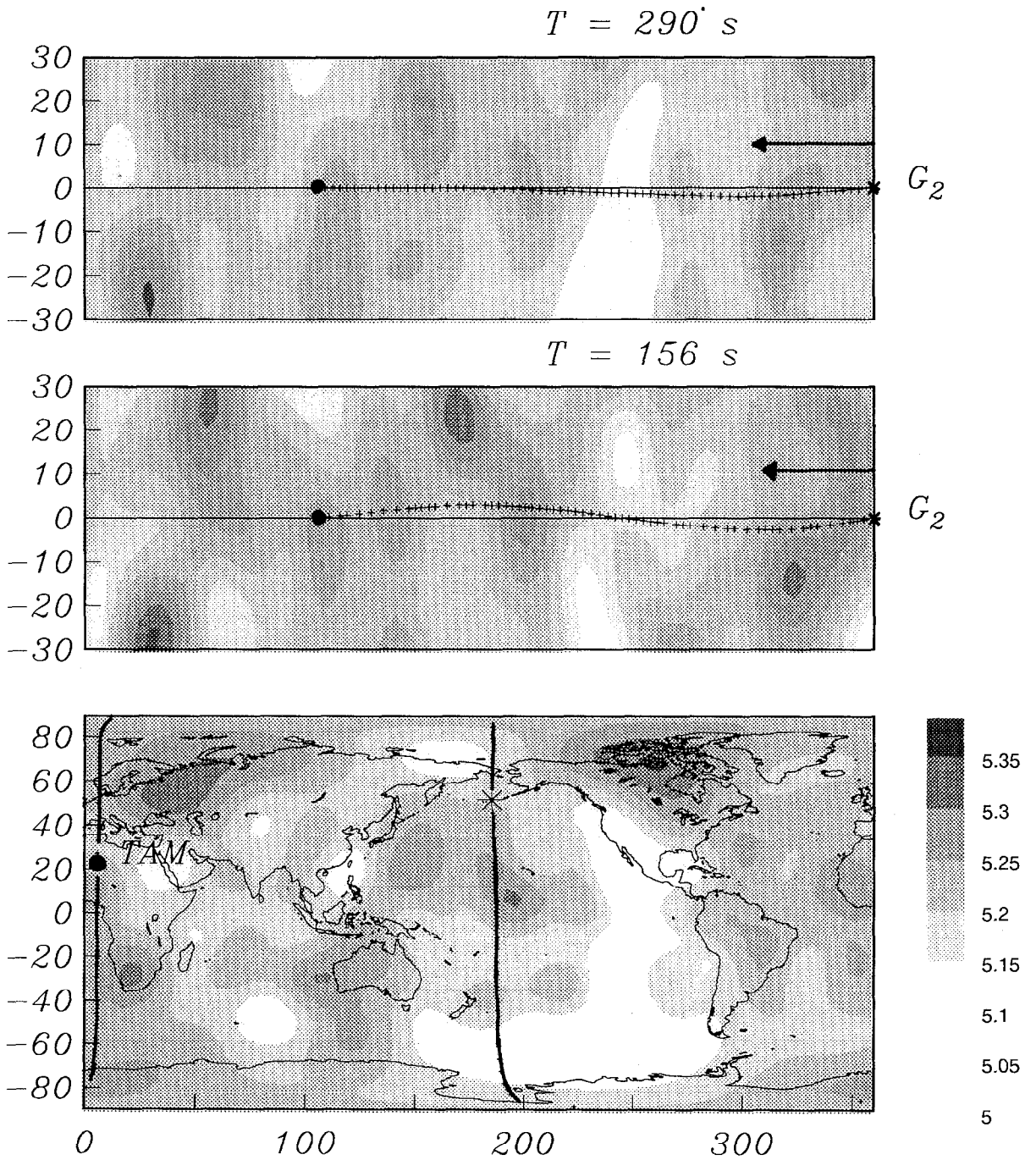

Fig. 9. Predicted ray path for G_2 obtained by exact ray tracing using the phase velocity models for modes ${}_0T_{26}$ and ${}_0T_{53}$ of Wong (1989). The great circle, which is shown in the lower panel together with the phase velocity map of mode ${}_0T_{26}$ (the station is marked by a dot, the source by an asterisk, and the velocities are given in km s^{-1}), is rotated onto the equator in the upper plots. Ray tracing predicts a horizontal azimuth of 0.4° for ${}_0T_{26}$ and −2.5° for ${}_0T_{53}$ for wave train G_1, and 0.5° (${}_0T_{26}$) and 2° (${}_0T_{53}$) for G_2. Prediction and measurements of Θ_{3H} show good agreement. For ${}_0T_{53}$ the ray is deflected from the great circle by 4°.

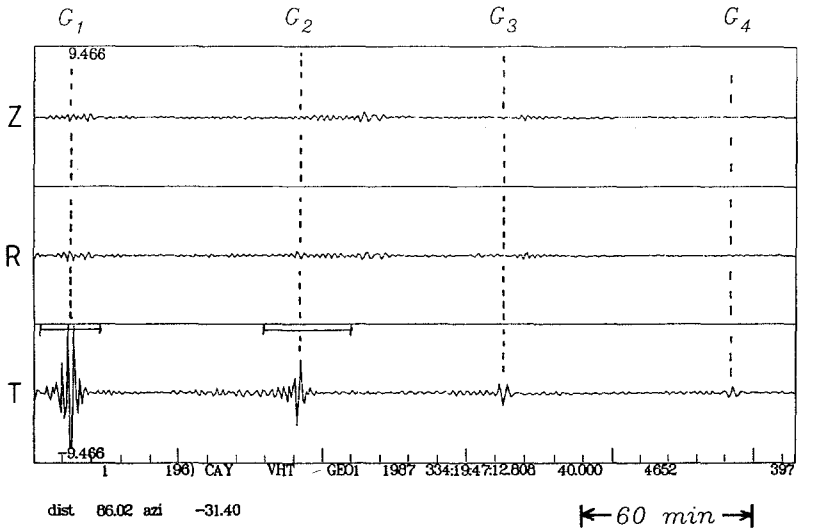

Fig. 10. Alaska earthquake (30 November 1987, 58.68°N, 142.79°W) recorded at GEOSCOPE Station Cayenne, French Guyana (CAY).The station is located at a node of the radiation pattern for Rayleigh waves, so the MTPA of the Love waves should not be biased strongly by the presence of other coherent signals.

with consequent changes in Θ_{3H} whereas the angle Θ_{2H} is not affected. For these reasons, we have chosen to interpret Θ_{2H} in the rest of this paper.

The second data example has the station located at a node of the radiation pattern of Rayleigh waves (Fig. 10), so the results of the polarization analysis for Love waves are less biased by interference with Rayleigh waves. The lengths of the multiple tapers for G_1 and G_2 were 20 min and 33 min, respectively, allowing three or four (for G_1) and five (for G_2) independent spectral estimates to be made in the frequency band 2–12 mHz. A large value of d_1 is characteristic of a well-defined polarization for G_1 and G_2, and ϵ and Θ_{3V} are indicative of linear polarization in the horizontal plane (Fig. 11). However, the polarization angle Θ_{3H} is significantly off by about $-5°$ on average for both G_1 and G_2.

5. Ray tracing experiments

To estimate the influence of aspherical velocity structure on the propagation of surface waves, ray tracing experiments were carried out and the expected ray azimuth arrival angles were evaluated for a given phase velocity map. Exact 2D ray tracing for surface waves on a sphere was performed by solving the ray equations as formulated by Woodhouse and Wong (1986). These workers described a method to estimate the initial take-off angle of the ray which can be used as starting value in the shooting method of solution. In their linear path integral approximation, the phase Ψ the amplitude A, and the off-azimuth arrival direction ν are calculated in terms of an integral along the unperturbed great circle path correct to first order in the phase velocity heterogeneity. As ν depends only on the gradient transverse to the ray, it is convenient to rotate the source–receiver great circle into the equator. In the new coordinate system, the off-azimuth arrival angle is, to first order,

$$\nu(\Delta) = -\left.\frac{\mathrm{d}\gamma}{\mathrm{d}\phi}\right|_{\phi=\Delta} \approx -\frac{1}{\sin\Delta}\int_0^{\Delta}\sin\phi\,\frac{\partial}{\partial\theta}\left[\frac{\delta c\left(\frac{\pi}{2},\phi\right)}{c_0}\right]\mathrm{d}\phi \tag{7}$$

with θ being the colatitude, ϕ the longitude, Δ the epicentral distance, $\gamma = \cot\theta$, $c = c(\theta,\phi)$ the phase velocity and ν the tangent of the arrival azimuth measured clockwise from the great circle. The arrival angle for multiple orbit wave trains becomes increasingly dominated by the integral along the whole great circle as the orbit number increases and so becomes insensitive to odd order structure. Accurate measurements for G_1, G_2, R_1 and R_2 are therefore essential for retrieving the complete phase velocity map. Finding undisturbed G_1 signals is particularly difficult, as their group velocities lie between those of the Rayleigh wave higher modes and the Rayleigh wave fundamental modes for periods $50 \leqslant T \leqslant 400$ s. This often means that short windows must be used, with a corresponding loss of frequency resolution.

In a first experiment, the measured ray azimuths for G_1, G_2 and R_1 of Fig. 6 are compared

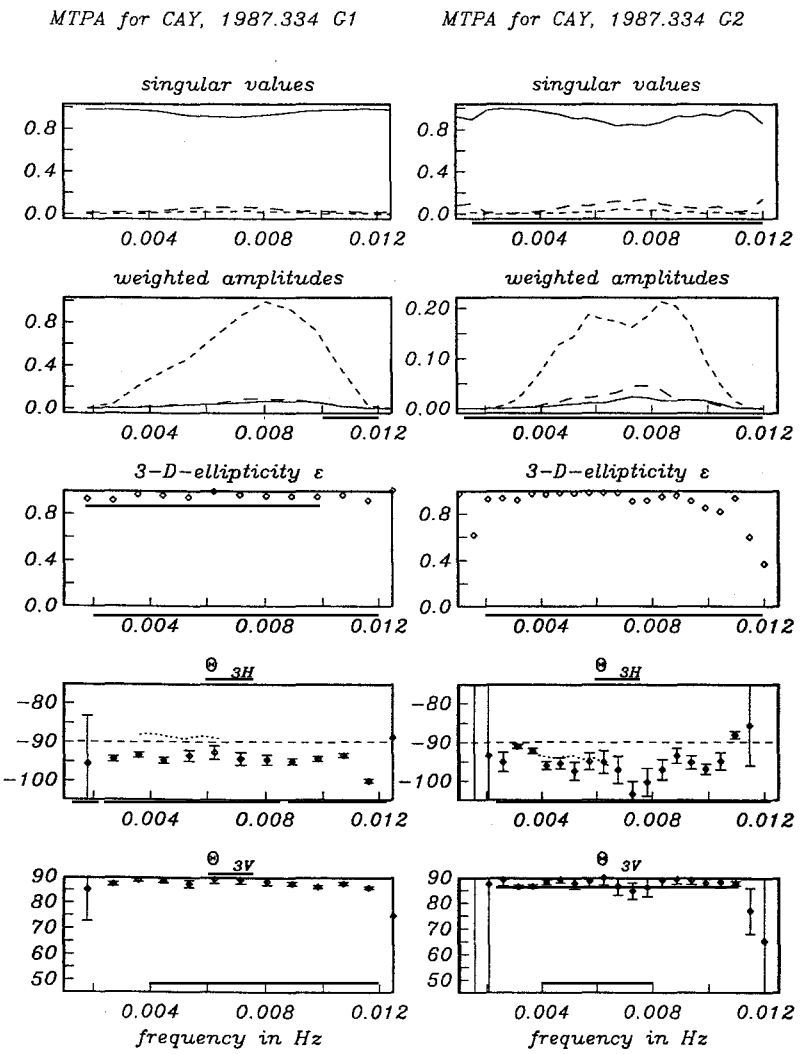

Fig. 11. MTPA results for G_1 and G_2. Although the singular values indicate the 'well-polarized case', the polarization angles show significant deviations from the transverse direction by as much as 5°, on average. (For further details, see Fig. 7.) Ray tracing results and measurements contradict each other for G_1 but agree well for G_2.

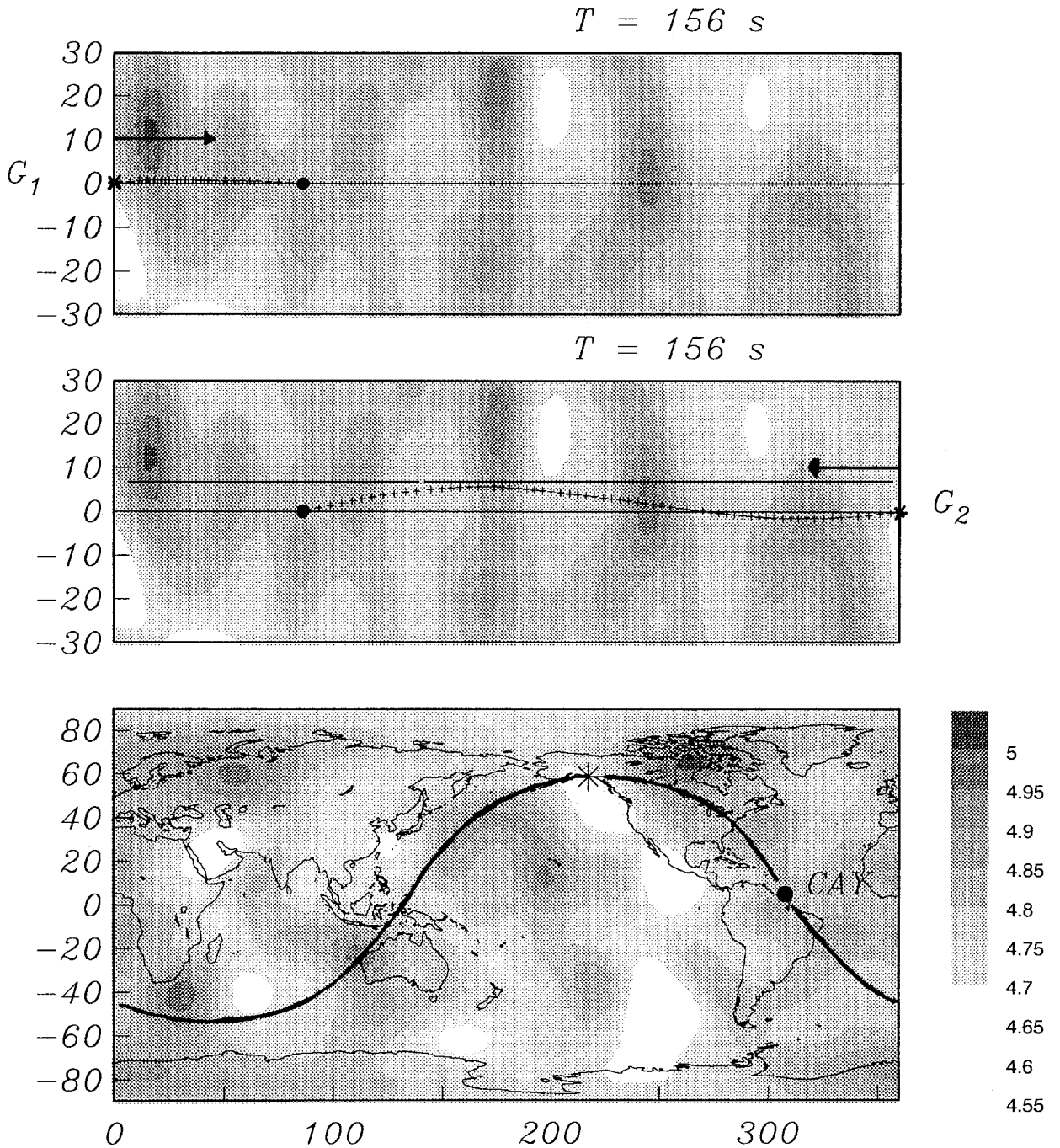

Fig. 12. Traced rays for G_1 and G_2 through Wong's (1989) phase velocity map for mode ${}_0T_{53}$. Whereas the measured anomalies in Θ_{3H} for G_1 seem to be significant and $-4°$ on average, ray tracing predicts an off-azimuth arrival angle of $+1.5°$. Prediction and measurement of Θ_{3H} for G_2 show good agreement. Whereas the measured anomaly is about $-6°$ (and the signal is significant), the ray tracing predicts an off-azimuth arrival angle of $-6.0°$. The ray of G_2 is deflected from the great circle by as much as 7°.

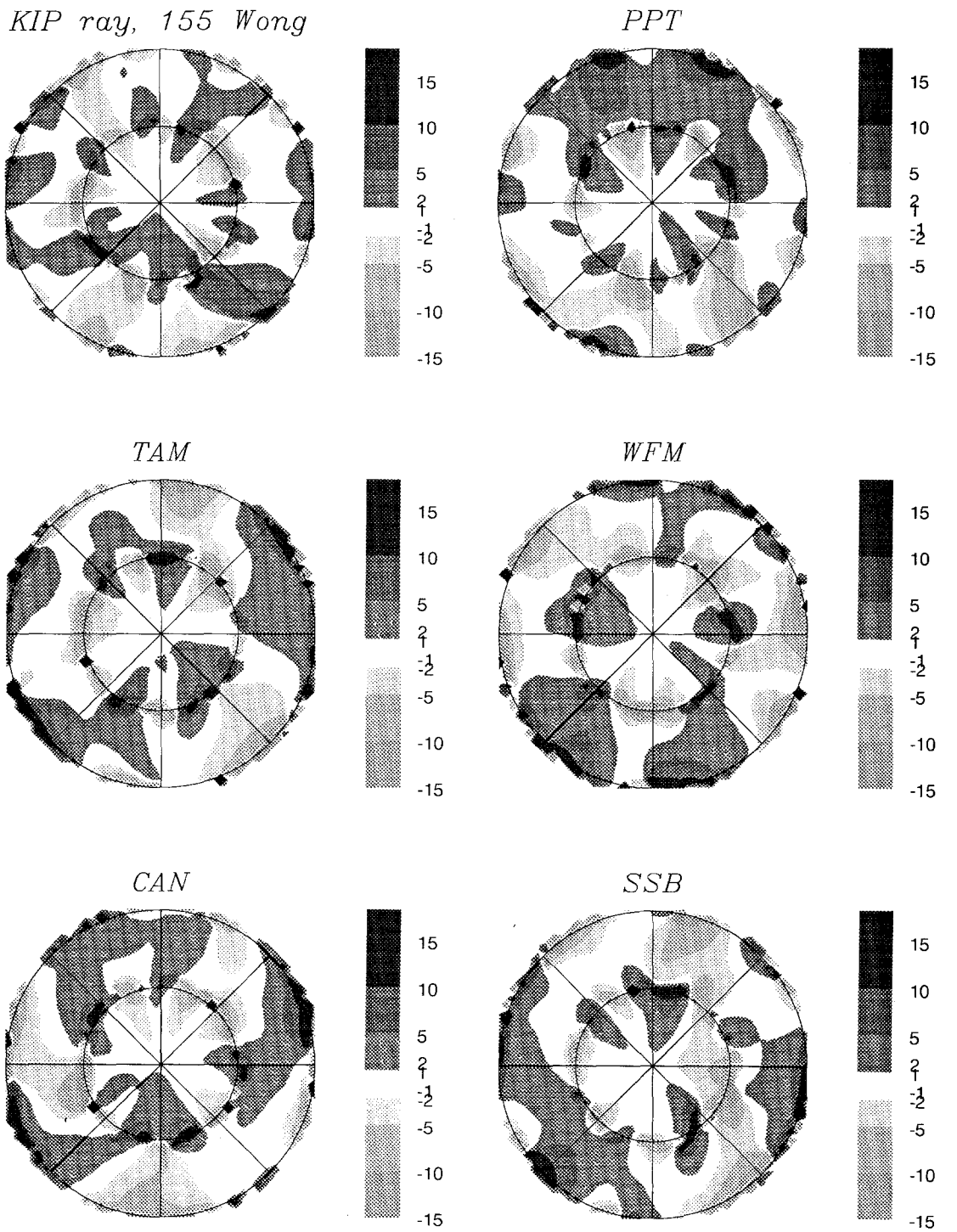

Fig. 13. Deviations of the theoretical arrival angles from the great circle directions at six of the GEOSCOPE stations shown in Fig. 5. The anomalies are plotted in a polar coordinate system with great circle azimuth α and total travel distance along the great circle Δ as parameters. The inner circle refers to results (shown in degrees) for R_1, and the outer to those for R_2. For better illustration, the sign of the angles for R_2 is flipped so that the patterns match when passing $\Delta = 180°$. For R_1, positive anomalies mean deviations to the right if looking along the great circle from the station to the fictive event.

a: GEOSCOPE ray (.80-1.0)

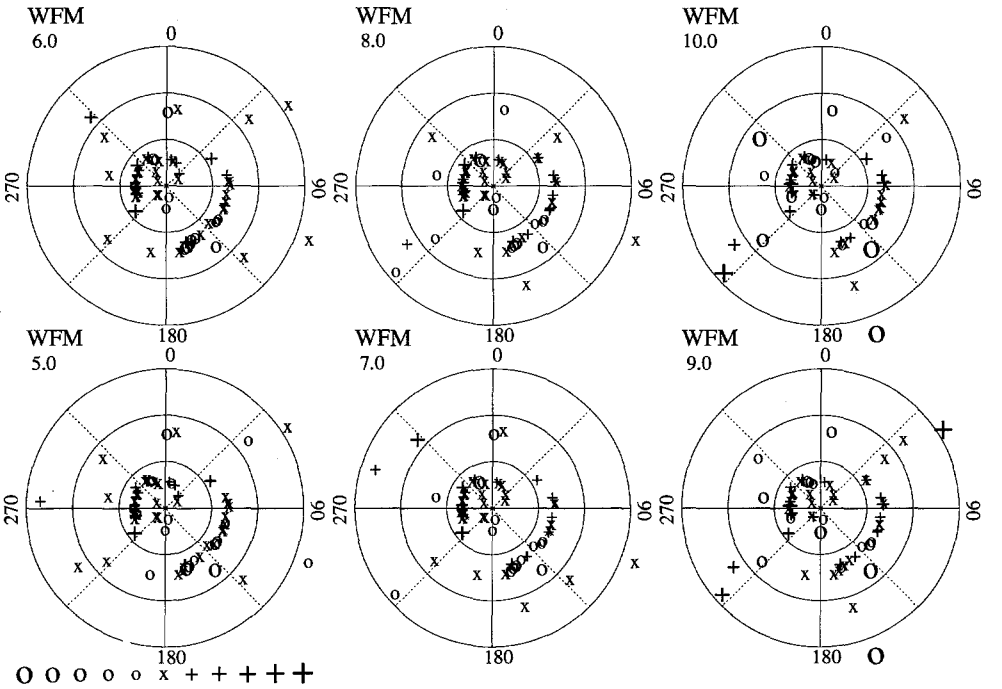

b: GEOSCOPE lov (.80-1.0)

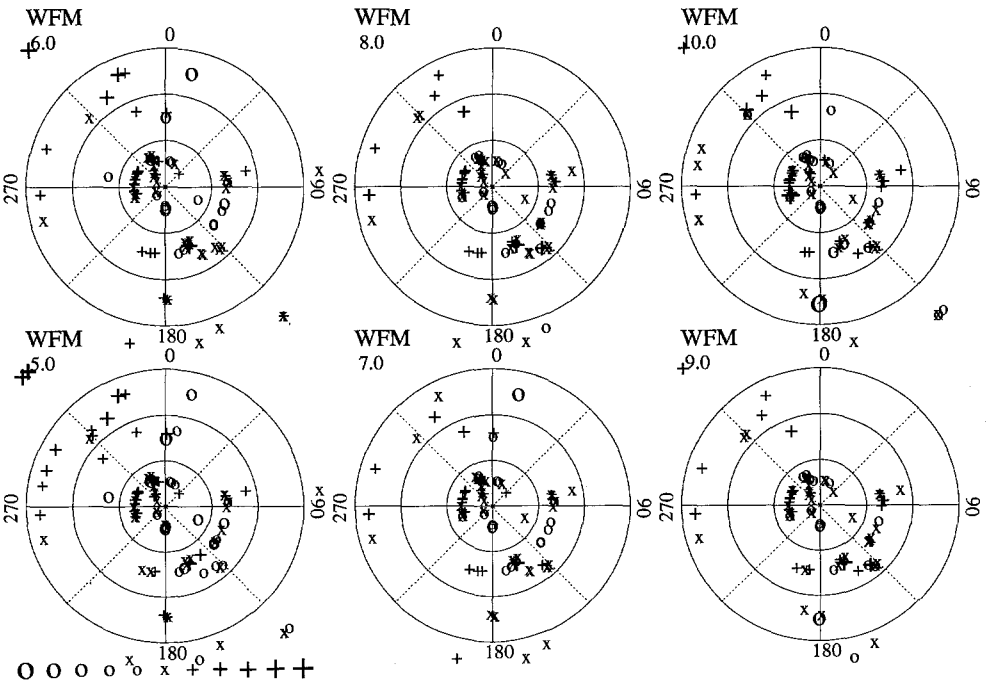

at mode periods between ${}_0T_{26}$ ($T = 290.559s$) and ${}_0T_{53}$ ($T = 156.094s$), and ${}_0S_{26}$ ($T = 289.695s$) and ${}_0S_{59}$ ($T = 155.504s$) to those angles obtained by ray tracing using the phase velocity models of Wong (1989). The source–receiver great circle is shown in the lower part of Fig. 9 together with the phase velocity map for ${}_0T_{26}$.The calculated ray azimuths for G_2 are 0.4° for ${}_0T_{26}$ and −2.5° for ${}_0T_{53}$, which is in reasonable agreement with the observations. The polarization angles calculated by ray tracing at the various modal frequencies listed by Wong (1989) are marked in Fig. 7 by the dotted line. The discrepancy between measured and theoretical polarization angles is not significant. The traced rays for G_1 are not shown here, but the results are also consistent with the measured angles (Fig. 7). For R_1, the ray tracing results are summarized in Fig. 8. There seems to be a significant discrepancy between measured and calculated ray azimuths. Even the frequency dependence shows an opposite trend.

For G_1 from the second event (Fig. 10), ray tracing using Wong's phase velocity model for ${}_0T_{53}$ predicts a ray azimuth of + 1.0°. The traced ray is shown in Fig. 12, together with the phase velocity map of ${}_0T_{53}$. In this example, the ray tracing results for G_1 do not agree with the measured angles at low frequencies, even though the measurements appear to be of good quality. In contrast to this observation, the measurements for G_2 agree well with the ray tracing results. Even the frequency dependence shows similar behaviour.

To show more clearly the effect of 3D structure on arrival angle at a particular station, we traced rays through Wong's (1989) degree 12 phase velocity map for mode ${}_0S_{59}$ ($T = 155.504s$) for six of the 10 stations of the GEOSCOPE network used in this study (Fig. 5). The resulting off-azimuth arrival angles are summarized in Fig. 13 as a function of the great circle azimuth and epicentral distance. The inner circle in Fig. 13 refers to calculations for R_1, and the outer to those for R_2. For R_1, dark shaded areas indicate positive anomalies (i.e. deviations to the right if looking from the station to the fictive event), and light shaded areas indicate negative anomalies. To avoid an apparent discontinuity of the ray azimuth in the plot at 180° distance, the sign of the angles for R_2 was flipped. It should be noted that the calculated off-azimuth arrival angles can have large magnitudes for epicentral distances close to 180°, which are probably due to the poorly defined great circle direction at the antipode and the presence of complicated caustics. Ray azimuths generally do not differ greatly from the great circle direction for short minor arcs. In some cases, however, large off-azimuth arrival angles are calculated even for small epicentral distances. At Stations CAN and KIP, rays approaching from the south are off by 5° even at 15° distance. The plots also show that the arrival angle usually varies slowly as a function of great circle azimuth and epicentral distance. For example, at Station PPT, the arrival angle of R_2 is between 2 and 10° for great circle azimuths from 315° to almost 90° at all distances. This implies that, generally, the variations of the polarization angles are smooth enough that the current distribution of sources and receivers will be adequate to constrain global phase-velocity maps without significant aliasing. In some cases, however, ray

Fig. 14. (a) MTPA results for Θ_{2H} measured at GEOSCOPE Station WFM. The analysis includes all very long period records of events from 1983 to 1989 with surface-wave magnitudes $M_s > 6.5$. The results (for various frequencies in the range 5–10 mHz which are indicated by numbers under the station name) are plotted as a function of great circle azimuth and epicentral distance, and are accepted only for largest singular values $d_1 > 0.80$. The inner circle refers to measurements for R_1, the middle circle to those for R_2; and the outer circle to those for R_3. The plus sign stands for horizontal azimuth deviations from the great circle to the right, and the o-sign for deviations to the left. The size of the symbols indicates the magnitude of the deviation in steps of 5°, so the largest symbols correspond to deviations of more than 20°. Insignificant deviations which are smaller than the measured error bars are marked by x. The measured values of Θ_{2H} are clearly dependent on the great circle azimuth. Certain 'patches' of the same symbol indicate consistency of different measurements. (b) The same as (a), for Love waves.

arrival angles change rapidly with great circle azimuth (e.g. KIP) and thus such behaviour should not be dismissed as a measurement artifact.

6. Preliminary results of a global analysis

A good coverage of measurements is necessary for inverting the observed ray azimuths into phase velocities. Moreover, the observations at each station for each frequency must be consistent. To compare predictions of the current phase velocity maps with polarization measurements, we analysed 81 large events ($M_s > 6.5$) from 1983 to 1989. Only shallow events have been chosen, to obtain wave packets of well-excited fundamental-mode surface waves and hence minimize the bias from interference with overtone wave packets. Figs. 14(a) and 14(b) summarize all measurements of Θ_{2H} with singular values $d_1 > 0.80$ at GEOSCOPE Station Westford, Massachusetts (WFM), for Rayleigh and Love waves. Each set of circles represents a particular frequency in the range 5.0–10.0 mHz. Θ_{2H} is plotted in a polar coordinate system with great circle azimuth α and epicentral distance Δ as parameters. The plus sign stands for significant deviation of the arrival azimuth from the great circle to the right, whereas the zero stands for deviation to the left when looking from station to event; the size of the symbols indicates the magnitude of deviation in steps of 5° and x marks insignificant deviations within the error bars. The measured values of Θ_{2H} are clearly dependent on great circle azimuth and distance over the whole frequency range. Certain 'patches' of the same symbol indicate consistency of different measurements. For frequencies between 5 and 6 mHz, the Rayleigh waves have negative or insignificant arrival anomalies over the whole range of great circle azimuth $90° \leqslant \alpha \leqslant 180°$ for R_2, whereas at higher frequencies increasingly positive deviations from the great circle are observed at these azimuths. Mainly positive arrival anomalies are measured for $225° \leqslant \alpha \leqslant 315°$ for R_1 at frequencies between 5 and 10 mHz, and negative anomalies dominate in the range 315–360°. The dependence of the polarization angle Θ_{2H} on frequency seems to be weak for low frequencies but becomes stronger for higher frequencies. Measurements for Love waves seem to be even more spatially coherent than those for Rayleigh waves.

For the chosen events, Θ_{2H} was also measured at the other GEOSCOPE stations of Fig. 5. The results at the frequencies of modes ${}_0S_{59}$ and ${}_0T_{53}$ are summarized in Figs. 15(a) and 15(b) for the six stations of Fig. 13. A good coverage of measurements is obtained for Stations WFM and

Table 1
Weighted average variances of the MTPA measurements (σ_0^2) and of the residuals compared with ray tracing results through Wong's (1989) phase velocity maps for Love and Rayleigh waves (σ_1^2)

Station	σ_0^2	σ_1^2	VR (%)	$P(F)$	$\bar{\epsilon}$	N	$\bar{\alpha}$	χ_0^2/N
Love waves, T = 156 s								
BNG	48.8	30.6	37	0.27	2.7	24	−1.7	16.6
CAN	14.9	10.5	29	0.16	3.1	67	−2.5	3.9
CAY	13.2	21.9	−66	0.15	3.5	34	−7.6	3.6
INU	26.8	30.0	−12	0.62	2.9	76	−3.2	7.2
KIP	11.5	22.9	−99	0.01	2.8	61	−0.9	3.4
PPT	51.1	34.3	33	0.27	2.8	32	−9.2	14.1
SCZ	50.1	30.5	39	0.07	2.9	56	−8.4	10.4
SSB	12.4	17.9	−45	0.28	3.2	36	−1.8	1.8
TAM	20.1	34.8	−73	0.13	3.0	33	−3.8	4.0
WFM	22.0	21.2	4	0.87	2.9	86	−2.6	5.1
Rayleigh waves, T = 155 s								
BNG	54.8	44.1	20	0.69	3.2	15	0.0	10.4
CAN	19.8	19.6	1	0.97	4.6	53	−2.6	2.5
CAY	58.2	51.6	11	0.80	4.7	20	−10.5	3.3
INU	36.8	34.1	7	0.77	4.7	59	−4.8	3.1
KIP	23.7	27.0	−14	0.68	4.0	43	−1.4	4.8
PPT	67.0	61.8	8	0.80	4.8	42	−10.9	8.1
SCZ	41.8	44.7	−7	0.81	4.7	55	−9.1	4.5
SSB	29.4	44.9	−53	0.23	4.7	34	−1.6	2.9
TAM	29.9	25.4	15	0.68	4.6	27	−6.7	2.3
WFM	40.8	35.3	13	0.55	4.5	71	−4.6	4.1

VR is the percentage variance reduction from the spherical to the heterogeneous model. $P(F)$ is the confidence level for the null hypothesis obtained in an F-test. It expresses the probability at which the two evaluated variances are significantly distinct (values close to zero) or similar (values close to one). $\bar{\epsilon}$ is the mean measurement error, N is the number of measurements and χ_0^2/N expresses the initial misfit of the data. If it is close to one or even smaller, then the model used (in this case a spherical model) can fit the data and no signal remains to be explained by changing the model. $\bar{\alpha}$ is the significant mean polarization anomaly.

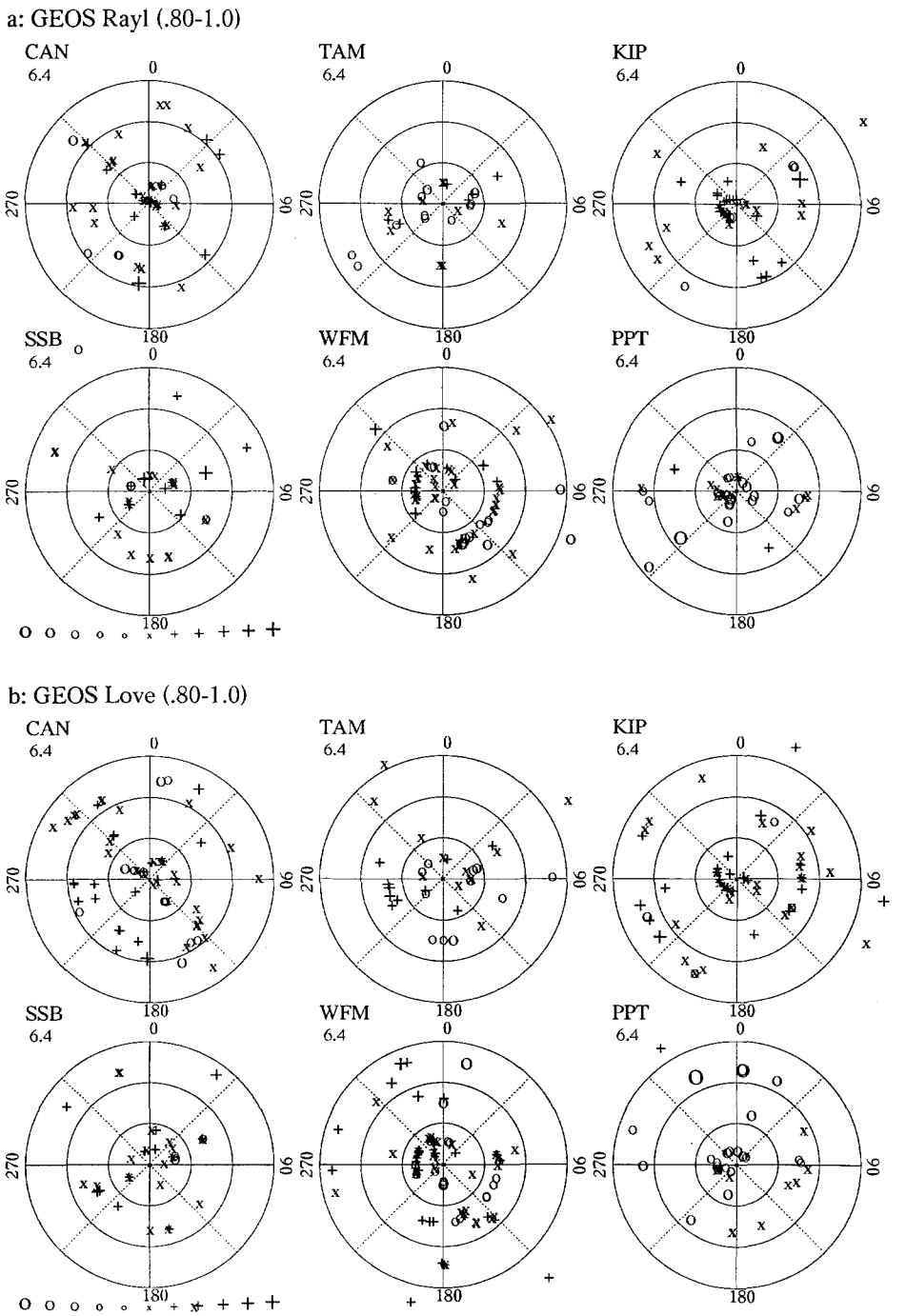

Fig. 15. (a) Measured ray azimuths obtained by the MTPA at the frequency of mode ${}_0S_{59}$ at Stations CAN, SSB, WFM, TAM, PPT and KIP. (For further details, see Fig. 14(a).) (b) The same as (a), for Love wave mode ${}_0T_{53}$. The coverage of measurements at Stations CAN and WFM is good, and arrival angles at CAN do not differ greatly from the great circle direction. At Station PPT, however, most measurements are negative for both Rayleigh and Love waves.

CAN. Some regions show good spatial coherency of the measurements, but there are also regions of rapid change and even some inconsistencies. The Love wave results do not vary greatly from the great circle direction at CAN, indicated by small symbols or an x, whereas Rayleigh wave measurements at SSB show larger variations. At Station CAN, some similarities between the pattern of measured angles and the pattern of the theoretical angles of Fig. 13 can be discerned. There are negative anomalies for R_1 at azimuths from 0° to 90° and for R_2 at azimuths close to 135° (it should be recalled that the sign for R_2 was flipped in Fig. 13). Measurements at Station PPT are anomalous. Love wave results are always negative and Rayleigh waves are off by negative angles in most cases. The azimuthal coverage of the measurements is good enough for us to conclude that a systematic shift to negative values exists at this location. This observation suggests that Station PPT might have some instrumentally induced problems, although it is also possible that strong local effects cause these anomalous patterns. If this apparent rotation of the North direction is actually caused by misalignment of the horizontal components, it can best be accounted for in a joint inversion for phase velocity and station orientation.

In Table 1, the weighted average variances and the variance reductions for Wong's maps are summarized. The variance reduction is positive for Love waves at Stations BNG, CAN, PPT and SCZ, although it should be mentioned that the values of the probability function $P(F)$ resulting from an F-test indicate that the variance reduction is significant with low confidence level and that it is not significant for Rayleigh waves. The measurements for Love waves at Stations TAM, CAY and KIP cannot be explained by the heterogeneous model (negative variance reduction with an 85% probability that the variances are different). The variance reduction is also negative for the Rayleigh wave measurements at stations SSB. For both wave types, the magnitude of the significant mean polarization anomaly is larger than 5° at Stations CAY, PPT and SCZ, where the major-

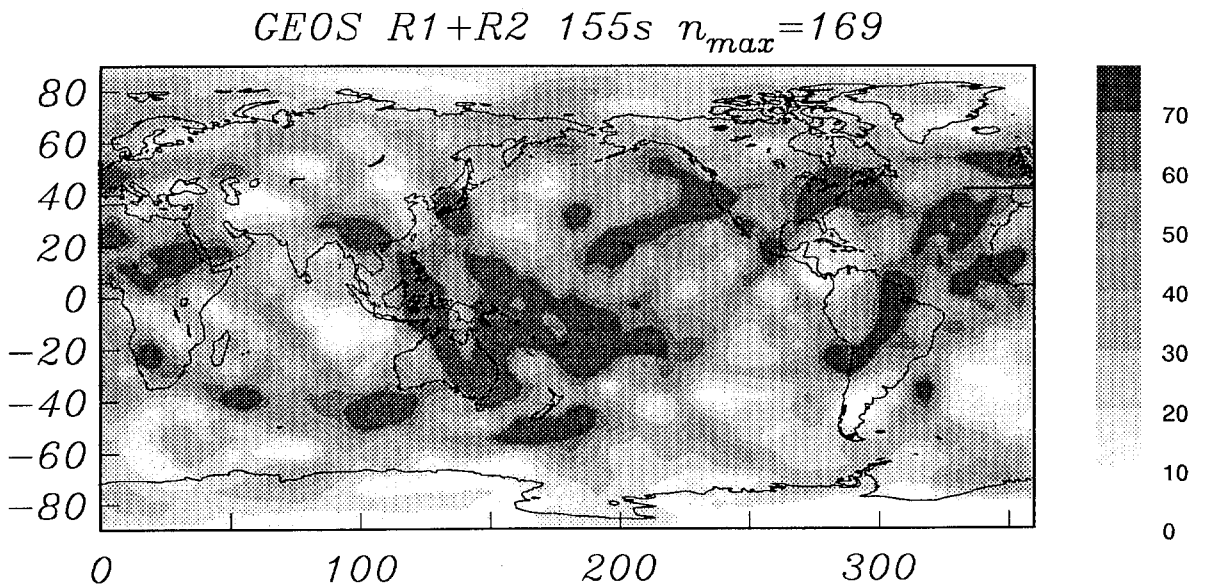

Fig. 16. Global coverage of the ray paths for R_1 and R_2 for the 10 stations used in this study expressed in a ray density plot. The rays were counted in sphericals caps of radius 5°. Relatively sparse coverage is achieved for the areas in the Indian Ocean, the northern part of Asia, the SE-Pacific Ocean and Antarctica.

ity of the measurements are negative (not shown for CAY and SCZ). This observation, together with that of Fig. 15, may indicate some misalignment problems of the horizontal components. As satisfying variance reduction cannot be achieved at all 10 stations, Wong's phase velocity maps need to be changed to fit our observations.

Fig. 16 shows the global coverage of the ray paths of R_1 and R_2 for the 10 stations used in this study. Although a denser ray coverage is desirable in the Indian Ocean, the northern part of Asia, the SE Pacific Ocean and Antarctica, we feel that the coverage of the measurements from the GEOSCOPE network is already adequate and an inversion can be carried out. Measurements at eight other stations of the GEOSCOPE network, which are not shown for simplicity, enhance the ray path coverage, and our database will be extended by measurements from the other global networks. The ray paths of the Love wave trains G_1 and G_2 are not shown here, but have a global coverage similar to that of the Rayleigh waves.

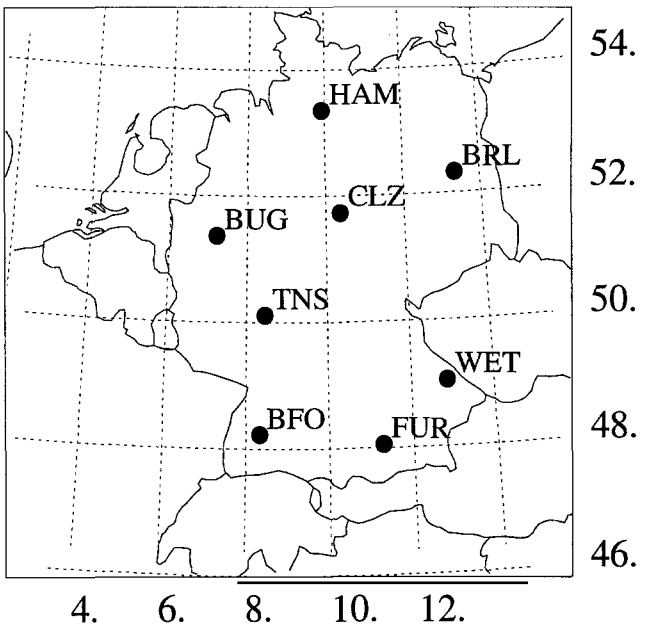

Fig. 17. Map of the German Regional Seismic broadband Network (GRSN) with the eight operating stations in the years 1991 and 1992.

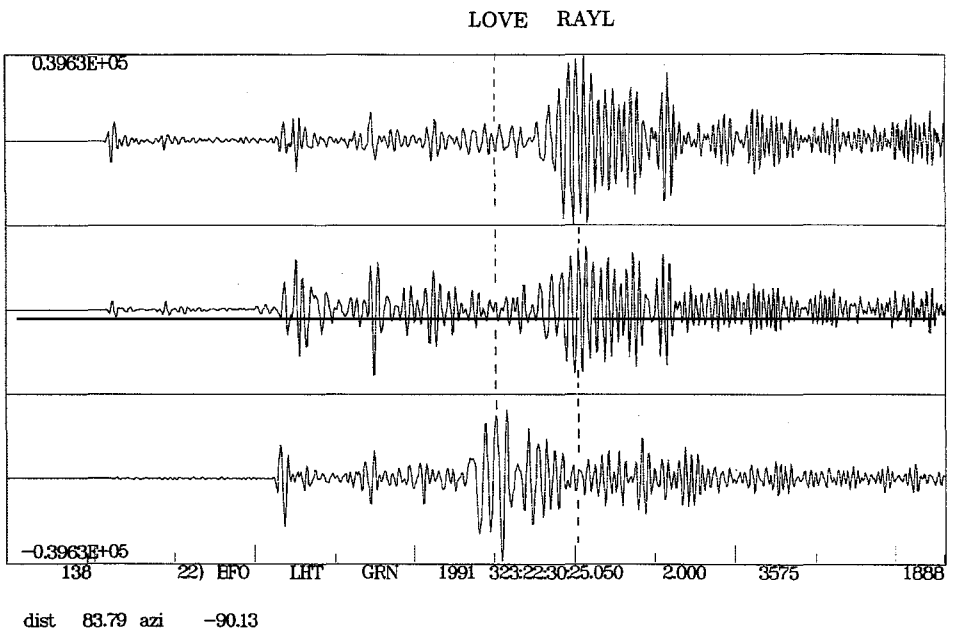

Fig. 18. Three-component seismogram (Z, R, T) of the Colombian earthquake (19 November 1991, 4.557°N, 77.485°W) recorded at the Black Forest Observatory, Schiltach (BFO), one of the stations of the German Regional Seismic Network (GRSN). The surface waves are clearly visible as the dominant signal in the seismogram. Even if the Love wave seems to be confined to the transverse component, the short-period part obviously overlaps in time with the long-period part of the Rayleigh wave. Hence a three-component MTPA for one wave type with a fixed location of the tapers in time is biased by the presence of the other wave type.

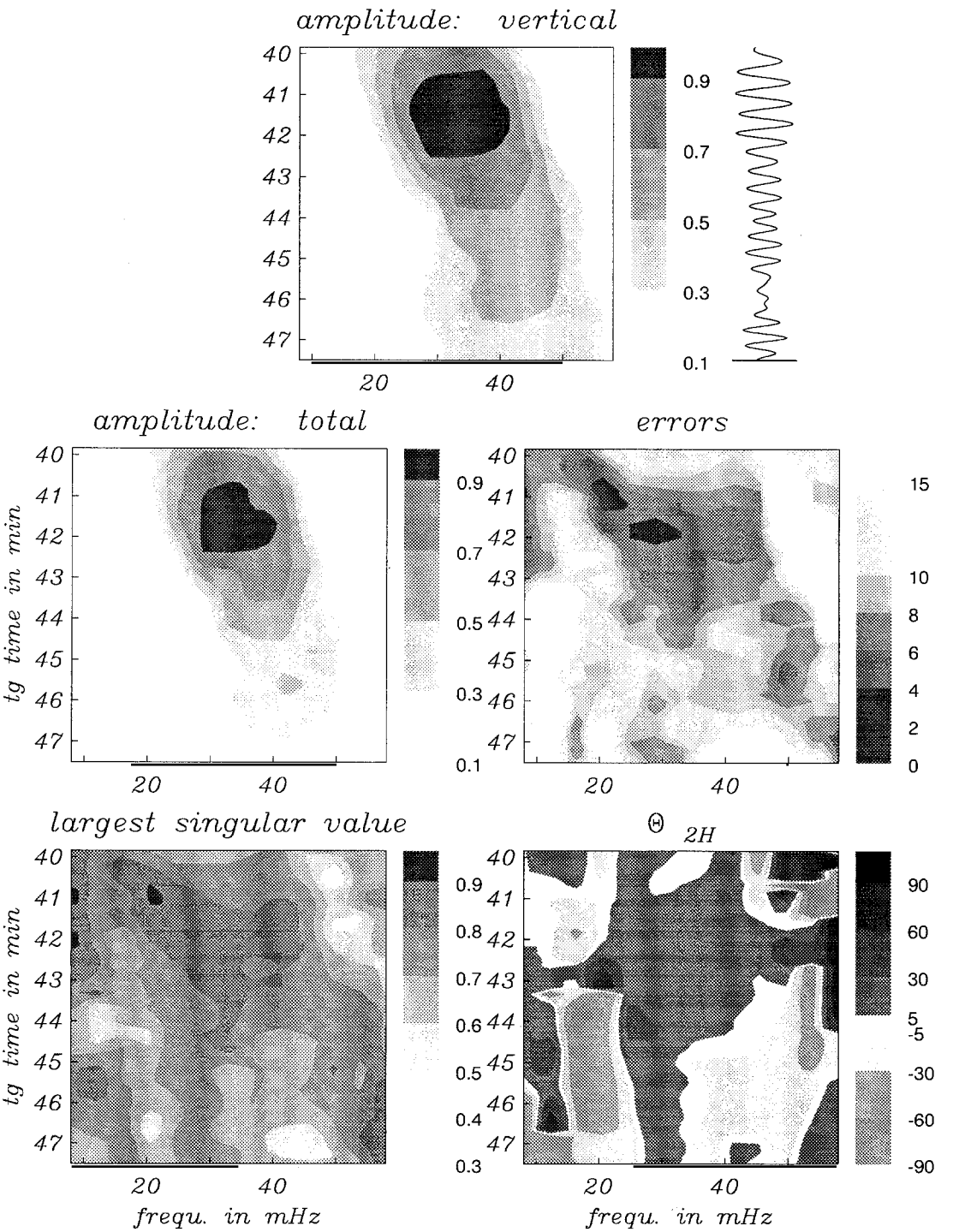
amplitude: vertical
amplitude: total
errors
largest singular value
Θ 2H
tg time in min
frequ. in mHz
BFO 19.11.91 R

7. Observations at the German Regional Seismic Network

In an experiment on a more regional scale, signals with frequencies between 10 and 60 mHz were analysed. A three-component seismogram (Z,R,T) recorded at BFO, a station of the German Regional Seismic broadband Network (GRSN) (Fig. 17) is shown in Fig. 18. The surface waves are clearly visible as the dominant signal in the seismogram. They appear to be well separated after rotation of the components to the nominal azimuth of the source. Love wave signals appear only on the transverse component, and Rayleigh wave signals only on the vertical and radial components, but the wave types overlap in time. The short-period Love waves have similar group travel times to the long-period Rayleigh waves, and the multi-taper technique, as it has been implemented in the global study, will give biased results. Pollitz and Hennet (1993) described a method for analysing signals which occur in the same time window of interest but do not overlap. They changed the tapers to suppress the Airy phase of the Love waves when the Rayleigh waves are analysed. We present a method which utilizes the dispersive nature of the surface waves. The signals of different wave type overlap but, owing to dispersion, they mostly have different frequencies in the time interval of interest (Fig. 18). The moving window method (Dziewonski and Hales, 1972) is the standard method for determining group and phase velocities of surface waves. We simply replace the usual single taper by the multi-tapers. For our experiment, a relatively short set of tapers (4 min long) with 3π frequency bandwidth yields three independent spectral estimates. The tapers are shifted successively through the seismogram, and the results are summarized in a matrix.

Fig. 19 shows the results for Rayleigh waves as a function of group travel time and frequency. The plot at the top shows the normalized amplitude on the vertical component. The strong dispersion of the wave packet is clearly visible. The corresponding seismogram section is drawn on the right. The middle panels show the total amplitude of the three-component seismogram $(A_Z^2 + A_R^2 + A_T^2)^{1/2}$ and the errors in the horizontal arrival azimuth Θ_{2H}. The lower panels show the largest singular value (d_1) and the arrival azimuth Θ_{2H}. Dark shaded areas indicate positive anomalies in Θ_{2H}, and lighter shaded areas indicate negative anomalies. The largest singular value is less than 0.8 for frequencies higher than 40 mHz, and the errors increase. For frequencies below 40 mHz, the largest singular values indicate a well-defined polarization with off-azimuth arrival angles between 5° and 30°. The final results for the angles can be read along the ridge of largest singular values. Owing to low signal levels, results for frequencies below 15 mHz should not be interpreted even though d_1 is very high. It is easy to see from an example such as this that any technique with a fixed window cannot provide the same accuracy as the moving window method, and it has been found that in some cases with strongly dispersed wave trains this method is also extremely useful when analysing long-period Rayleigh waves on the global scale.

To estimate the evolution of the wave front of R_1 and G_1 during their passage through the network, the wave front at each station is calculated from the polarization vector. The wave front, which is perpendicular to the ray if an isotropic velocity structure is assumed, is plotted at every GRSN station as a function of frequency (see Fig. 20(a) for R_1 and Fig. 20(b) for G_1). The results for G_1 become less accurate for frequencies higher than 30 mHz. The wave fronts are clearly

Fig. 19. MTPA results for the Rayleigh wave train R_1 for the seismogram shown in Fig. 18 as a function of frequency and group travel time, tg. The MTPA was performed by shifting the set of tapers in a moving window technique through the seismogram. The dispersive nature of R_1 is clearly visible in the amplitude plots. The largest singular values, the horizontal azimuths Θ_{2H} and the errors in Θ_{2H} (in degrees) are also shown. Θ_{2H} seems to be frequency dependent. However, a decreasing largest singular value at high frequencies indicates probable bias by other signals.

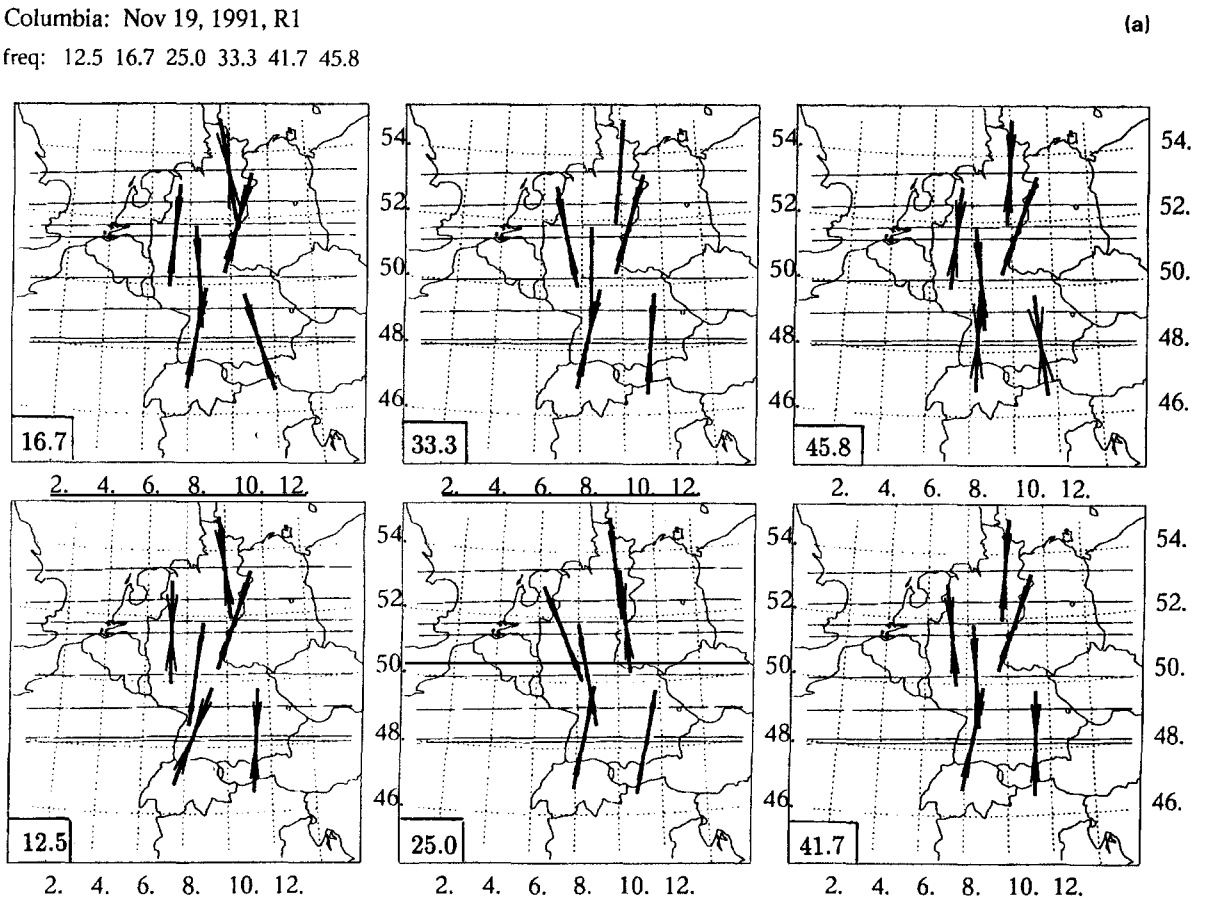

Fig. 20. (a) Results for Θ_{2H} of R_1, recorded at the GRSN stations are used to reconstruct the approaching wave front for different frequencies (in mHz in the lower left corner of each map). The errors in Θ_{2H} are indicated by smaller bars. The wave front is distorted when passing through the GRSN array. This indicates the presence of lateral heterogeneities within the array. (b) The same as (a), for Love waves. As the patterns for Rayleigh waves and Love waves show consistency, it is expected that the phase velocity maps will show similar patterns.

distorted during their passage through the GRSN array. This indicates the presence of lateral phase velocity variations within the array. Except for frequency 16.7 mHz, the southern stations (BFO and FUR) generally show consistent directions which are significantly different from those of the northern stations. A possible cause might be a distortion of the wave fronts as a result of scattering of the surface waves by the Alps in the south. Large variations between adjacent stations (e.g. HAM and BRL) lead to the suggestion that strong local effects might be present as well. The azimuth of the wave front shows rapid variations with frequency. At Station BUG the azimuth varies by 10° for frequencies from 25 to 33 mHz. The same phenomenon is observed at Stations TNS, HAM and BRL. The results for G_1 show similar behaviour to those for R_1, which indicates that the phase velocity maps must show similar patterns.

8. Concluding remarks

Current maps of surface wave dispersion agree fairly well in shape at harmonic degrees lower

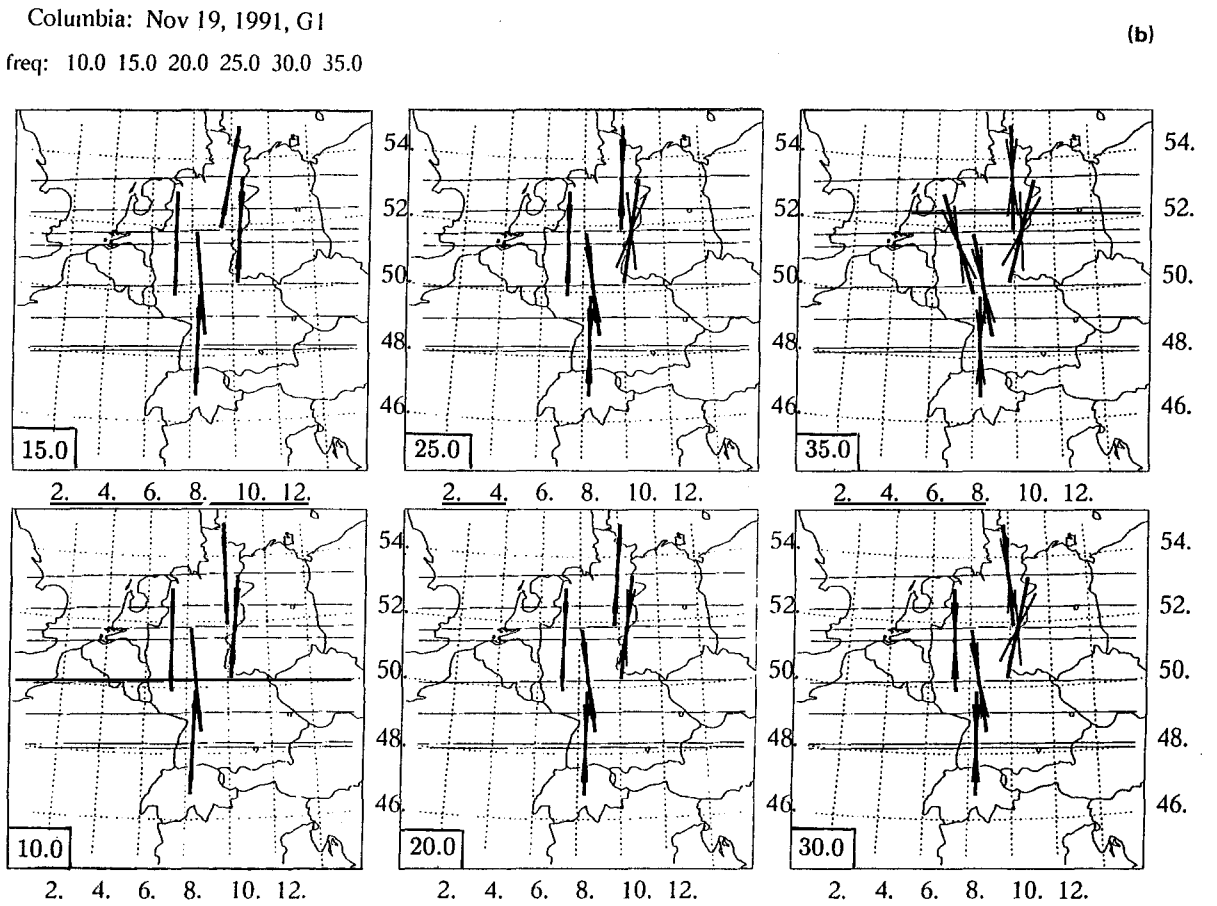

Fig. 20 (continued).

than seven or eight, but vary significantly in amplitude. Furthermore, higher-degree structure is very variable from researcher to researcher. Surface-wave polarization data can be used to improve this situation, and this paper presents a preliminary dataset measured from recordings of the GEOSCOPE network. These data can be used to constrain global phase velocity maps, and are particularly helpful in constraining higher-order structure as they are sensitive to the lateral gradient of phase velocity. We have demonstrated that reliable measurements of the frequency dependence of polarization angles can be made using a multi-taper technique. Surface-wave ray tracing shows that the current phase velocity maps go some way to modelling the measurements but that much signal remains to be explained. A few stations show peculiar patterns of polarization angles which may be due to an instrumental defect or to the presence of strongly anomalous structure in the vicinity of the installation. It is also important to realize that anisotropy may be an important contributor to polarization anomalies. Anisotropy has already been invoked in the inversion of long-period phase velocity data (Montagner and Tanimoto, 1991) and to explain some polarization anomalies in relatively short-period data (Vig and Mitchell, 1990). It has recently been proposed that large-scale anisotropic structures must be present to explain some observations of long-period quasi-Love and quasi-Rayleigh waves (Park and Yu, 1992). By defini-

tion, such waves are accompanied by large polarization anomalies, and it is important to determine if anisotropy is the major cause of such signals. We anticipate that a combination of modelling experiments using synthetic seismograms and the analysis of a global dataset of polarization measurements will go a long way to resolving this issue.

We have also experimented with regional-scale problems using data from the German Regional Seismic Network. A multi-taper moving window polarization analysis serves to separate surface-wave signals of different frequency which overlap in group arrival time. The analysis reveals strong distortion of surface-wave wave fronts as they cross the network, and such measurements will provide useful constraints in the numerical modelling of regional surface-wave propagation. The moving window analysis may also be useful in global studies at periods longer than 50 s for travel paths which cause significant dispersion.

The next step in our research is the inclusion of the polarization data in a formal inversion for phase velocity (Woodhouse and Wong, 1986; Hu and Menke, 1992). The current density of measurements is already sufficient to allow an inversion, but the results will be strengthened by adding further data from the GEOSCOPE array and other high-quality three-component global networks.

Acknowledgements

We thank the GEOSCOPE project team at Institut Physique de Globe de Paris, for courteously making available the data used in this study. We thank Jim Mechie for carefully reading the manuscript and for many helpful discussions. We also thank Harold Bolton for patiently supporting us in the data processing. We are grateful to Erhard Wielandt, Ruedi Widmer and the MODES working group of the Geophysical Institutes at Karlsruhe and Stuttgart for many lively discussions on long-period seismology. This research was supported by National Science Foundation Grant EAR-90-04555 and by the programme 'Stress and Stress Release in the Lithosphere' at the University of Karlsruhe, sponsored by the Deutsche Forschungsgemeinschaft (SFB 108, Contribution 402).

References

Dziewonski, A.M. and Hales, A.L., 1972. Numerical analysis of dispersed seismic waves. In: B.A. Bolt, B. Alder, S. Fernbach and M. Rotenberg (Editors), Methods in Computational Physics, Vol. 11. Academic Press, New York, pp. 39–85.

Horn, R.A. and Johnson, C.R., 1991. Matrix Analysis. Cambridge University Press, Cambridge, 561 pp.

Hu, G. and Menke, W., 1992. Formal inversion of laterally heterogeneous velocity structure from *P*-wave polarization data. Geophys. J. Int., 110: 63–69.

Jurkevics, A., 1988. Polarization analysis of three-component array data. Bull. Seismol. Soc. Am., 78: 1725–1743.

Keilis-Borok, V.I., 1989. Seismic Surface Waves in a Laterally Inhomogeneous Earth. Kluwer Academic, Dordrecht.

Lay, T. and Kanamori, H., 1985. Geometric effects of global lateral heterogeneity on long-period surface wave propagation. J. Geophys. Res., 90: 605–622.

Lerner-Lam, A.L. and Park, J.J., 1989. Frequency-dependent refraction and multipathing of 10–100 second surface waves in the Western Pacific. Geophys. Res. Lett., 16: 527–530.

Masters, G., Priestley, K.F. and Gilbert, F., 1984. Observations of off-path propagation on horizontal component low frequency seismograms. Terra Cognita, 4: 250.

Masters, G., Bolton, H. and Shearer, P., 1992. Large-scale 3-dimensional structure of the mantle. EOS, Trans. Am. Geophys. Union, 73: 201.

Montagner, J.-P. and Tanimoto, T., 1990. Global anisotropy in the upper mantle inferred from the regionalization of phase velocities. J. Geophys. Res., 95: 4797–4819.

Montagner, J.-P. and Tanimoto, T., 1991. Global upper mantle tomography of seismic velocities and anisotropies. J. Geophys. Res., 96: 20337–20351.

Park, J. and Yu, Y., 1992. Anisotropy and coupled free oscillations: simplified models and surface wave observations. Geophys. J. Int., 110: 401–420.

Park, J., Lindberg, C.R. and Vernon, III, F.L., 1987a. Multitaper spectral analysis of high-frequency seismograms. J. Geophys. Res., 92: 12675–12684.

Park, J., Vernon, III, F.L. and Lindberg, C.R., 1987b. Frequency dependent polarization analysis of high-frequency seismograms. J. Geophys. Res., 92: 12664–12674.

Paulssen, H., Levshin, A.L., Lander, A.V. and Snieder, R., 1990. Time- and frequency-dependent polarization analysis: anomalous surface wave observations in Iberia. Geophys. J. Int., 103: 483–496.

Pollitz, F.F. and Hennet, C.G., 1993. Analysis of Rayleigh wave refraction from three-component seismic spectra. Geophys. J. Int., 113: 629–650.

Romanowicz, B., Cara, M., Fels, J.F. and Roult, G., 1984. GEOSCOPE; a French initiative in long period three component global seismic networks. EOS, Trans. Am. Geophys. Union, 65: 753–756.

Samson, J.C., 1983a. Pure states, polarized waves, and principal components in the spectra of multiple, geophysical time-series. Geophys. J.R. Astron. Soc., 72: 647–664.

Samson, J.C., 1983b. The spectral matrix, eigenvalues and principal components in the analysis of multichannel geophysical data. Ann. Geophys., 1(2): 115–119.

Slepian, D., 1978. Prolate spheroidal wave functions, Fourier analysis, and uncertainty. V: The discrete case. Bell Syst. Tech. J., 57: 1371–1430.

Su, W., Woodward, R.L. and Dziewonski, A.M., 1992. Deep origin of mid-oceanic ridge velocity anomalies. Nature, 360: 149–152.

Thomson, D.J., 1982. Spectrum estimation and harmonic analysis. IEEE Proc., 70: 1055–1096.

Vidale, J.E., 1986. Complex polarization analysis of particle motion. Bull. Seismol. Soc. Am., 76: 1393–1405.

Vig, P.K. and Mitchell, B.J., 1990. Anisotropy beneath Hawaii from surface wave particle motion observations. Pure Appl. Geophys., 133: 1–22.

Wong, Y.K., 1989. Upper mantle heterogeneity from phase and amplitude data of mantle waves. Ph.D. Thesis, Harvard University, Cambridge, MA.

Woodhouse, J.H. and Dziewonski, A.M., 1984. Mapping of the upper mantle: three-dimensional modeling of earth structure by inversion of seismic waveforms. J. Geophys. Res., 89: 5953–5986.

Woodhouse, J.H. and Wong, Y.K., 1986. Amplitude, phase and path anomalies of mantle waves. Geophys. J.R. Astron. Soc., 87: 753–773.

Woodward, R.L., Forte, A.M., Su, W. and Dziewonski, A.M., 1993. Constraints on the large-scale structure of the Earth's mantle. In: E. Takahashi, R. Jeanloz and D. Rubie (Editors), Evolution of the Earth and Planets, Geophysical Monograph 74, IUGG Vol. 14, Int. Union of Geodesy and Geophysics and American Geophysical Union, Washington DC.

Zhang, Y.-S. and Tanimoto, T., 1992. Ridges, hotspots and their interactions as observed in seismic velocity maps. Nature, 355: 45–49.